# Nanotexture and crystal phase regulation for synergistic enhancement in re-endothelialization on medical pure titanium surface

Jing Zhang [a],[1], Kai Ren [b],[1], Jingru Qiu [c], Baolan Chen [a], Weixun Duan [b], Jincheng Liu [b],[***], Guiling Li [a],[**], Donghai Li [a],[*]

[a] *Advanced Medical Research Institute, Meili Lake Translational Research Park, Cheeloo College of Medicine, Shenzhen Research Institute of Shandong University, Shandong University, Jinan, Shandong, PR China*
[b] *Department of Cardiovascular Surgery, Xijing Hospital, Air Force Military Medical University, Xi'an, Shaanxi, PR China*
[c] *Department of Medicinal Chemistry, Key Laboratory of Chemical Biology (Ministry of Education), School of Pharmaceutical Sciences, Cheeloo College of Medicine, Shandong University, Jinan, Shandong, PR China*

## A B S T R A C T

Re-endothelialization has been recognized as a promising strategy to address the tissue hyperplasia and subsequent restenosis which are major complications associated with vascular implant/interventional titanium devices. However, the uncontrollable over-proliferation of smooth muscle cells (SMCs) limits the clinical application of numerous modified strategies. Herein, a novel modified strategy involving with a two-step anodic oxidation and annealing treatment was proposed to achieve rapid re-endothelialization function regulated by regular honeycomb nanotexture and specific anatase phase on the titanium surface. Theoretical calculation revealed that the presence of nanotexture reduced the polar component of surface energy, while the generation of anatase significantly enhanced the polar component and total surface energy. Meanwhile, the modified surface with regular nanotexture and anatase phase produced positive effect on the expression of CD31, VE-Cadherin and down-regulated α-SMA proteins expression, indicating excellent capacity of pro-endothelial regeneration and inhibition of SMCs proliferation and migration. One-month *in vivo* implantation in rabbit carotid arteries further confirmed that modified tube implant surface effectively accelerated confluent endothelial monolayer formation and promoted native-like endothelium tissue regeneration. By contrast, original titanium tube implant induced a disorganized tissue proliferation in the lumen with a high risk of restenosis. Collectively, this study opens us an alternative route to achieve the function that selectively promotes endothelial cells (ECs) growth and suppresses SMCs on the medical titanium surface, which has a great potential in facilitating re-endothelialization on the surface of blood-contacting titanium implant.

## 1. Introduction

Coronary artery disease, as a chronic inflammatory cardiovascular disease that seriously threatens human health, is caused by the accumulation of fatty deposits in the coronary arteries leading to arterial narrowing [1,2]. The advent of percutaneous coronary intervention has brought hope to millions of patients with coronary artery disease. However, implantation of cardiovascular devices often causes adverse effects such as thrombosis and restenosis and leads to implant failure, which is mainly attributed to endothelial damage caused by implantation, delayed endothelialization due to non-specific interactions of antiproliferative drugs, and inadequate biocompatibility of matrix material [3,4]. As an internal barrier, the endothelium plays a vital role in several physiological and pathological processes, including vascular development and remodeling [5]. Endothelial damage will trigger excessive proliferation of smooth muscle cells, platelet activation, and so on, ultimately leading to a series of vascular diseases such as intimal hyperplasia and thrombosis [6,7]. Thus, promoting endothelialization

---

on vascular material surface by selectively favoring endothelial cells growth and inhibiting smooth muscle cells is considered as one of the most promising strategies in tissue engineering applications [8–12].

Currently, different modified strategies were proposed to maximize the rapid endothelialization and suppress tissue disorderly hyperplasia on the implant surfaces, such as surface bioactive modification and inert modification (physicochemical modification) [13–15]. Among them, bioactive strategy acted by immobilizing cell adhesion proteins or peptides on the biomaterial surfaces to promote the attachment and proliferation of endothelial cell, such as extracellular matrix-derived cell-selective peptides like YIGSR and REDV which act via direct interaction with integrin receptors onto the endothelial cell surface [16–19]. However, the number of endothelial cell-selective peptides that can be applied is very limited until now. Moreover, these active peptides usually face some problems including poor stability against enzymatic degradation, susceptibility to functional inactivation, long synthesis time, and difficulty in mass preparation, which greatly limit their widespread applications [20].

Unlike the bioactive modification strategy, inert modification strategy is considered as a stable and promising surface modification approach, where the proliferation behaviors of endothelial cells and smooth muscle cells usually are regulated by controlling the surface properties such as topography, chemical composition, wettability, crystalline phase, etc [21–23]. Titanium and its alloys are broadly applied in the various implantable/interventional medical devices due to its great physicochemical properties and biocompatibility, which is largely dependent on the oxide layer formed on the surface when exposed to air- or oxygen-containing solution [24]. It has been demonstrated that $TiO_2$ is a promising biomaterial with good biological activity and responses, which is usually proposed as suitable inorganic coating for bare metal implants [25–28]. At present, some $TiO_2$ coatings with nanomorphology have been widely reported, such as $TiO_2$ nanotube, nanowire, nanoparticle, and nanorod, which showed great potential beneficial in modulating the biological response of endothelial cells, smooth muscle cells, and platelets due to special micromorphology [22, 29–31]. On one hand, the nanomorphology can directly regulate the absorption behavior of typical functional proteins with nanoscale size in extracellular matrix, which in turn affected its binding to specific receptor and subsequently cell response [32]. One the other hand, nanotexture with the dimension close to some important transmembrane receptors, such as integrin, contact-induced conformational changes in transmembrane proteins dependent on nanoscale morphology might trigger corresponding signaling pathway and direct cells adhesion or migration behaviors [33,34]. For example, $TiO_2$ nanotubes layers with a pore size of 90–110 nm can effectively promote endothelial cells growth while inhibiting smooth muscle cells migration, the special biological effect induced by nanomorphology provides a new strategy to improve the hemocompatibility of titanium [31,35]. However, these $TiO_2$ nanotexture surface face a problem, i.e., the poor strength of the nanotextures and the bonding strength with the substrate, which hindered its further application in the blood-contacting medical devices.

Additionally, crystal phase of $TiO_2$ was also closely related to cells adhesion and proliferation. The favorable biocompatibility of $TiO_2$ is also attributed to the n-type semiconductor properties and the difference in surface energy induced by different crystal phase (anatase and rutile) [21,36]. Compared with amorphous titanium, an enhanced endothelialization and bioactivity levels of the material surface with anatase and rutile were preliminarily confirmed. Anatase has a large band gap (3.2 eV) than rutile (3.0 eV), and when the energy (photo energy) absorbed into the material surface is greater than the band gap of crystal phase, electrons were transmitted from the valence band to the conduction band generating electron-hole pairs. The electron-hole with strong oxidizing ability could react with water molecular to generate active groups such as –OH and $O_2^-$. These active groups could react with biomolecules inside the cells, further affecting the response behaviors of cells [37]. For example, recent studies showed that anatase could

enhance the adhesion of endothelial cells through the upregulation of various adhesion molecules while rutile seem to have litter effects on proliferation of endothelial cells [30]. Although the awareness that morphology or crystal phase of $TiO_2$-based biomaterials has an impact on the biological behaviors of endothelial cells and smooth muscle cells is recognized by all, the intrinsic regulatory mechanism is currently unclear due to the difference in reference surface, measurement methods involved in the experiments, giving rise to a range of inconsistent views [38]. In particular, the synergistic regulation mechanism of nanomorphology and crystal phase on biological response is still missing. Therefore, more systematic *in vitro* and *in vivo* experiments should be performed to deeply reveal the biological effect induced by morphology and crystal phase with the help of protein expression and cell morphology analysis.

Here, a novel strategy for fabricating the highly organized and robust nanotexture on titanium substrate was proposed by a two-step anodic oxidation, combining with an annealing treatment to achieve a precise regulation of nanotexture topography and crystal phase of $TiO_2$. The wettability and surface energy of different samples surface were characterized and calculated based on the complete Young-equation, theoretical calculation revealed that the presence of nanotexture reduced the polar component of surface energy, while the generation of anatase significantly enhanced the polar component and total surface energy. *In vitro* and *in vivo* experiments revealed that synergistic regulation of nanotexture and anatase could accelerate confluent endothelial monolayer formation and promote native-like endothelium tissue regeneration (Fig. 1).

## 2. Experimental section

### 2.1. Materials

Medical pure titanium (TA1, Baoji Dexin Titanium Co.,Ltd) sheets of 0.1 mm thickness were cropped to the appropriate size of 10 mm × 15 mm. To clear the surface oxidized layer and smooth the titanium sheet surface, they were washed in ultrasonic bath with an acid solution of 0.66 *wt*% hydrofluoric acid (HF, AR, Macklin) and 0.8 *wt*% nitric acid (HNO$_3$, AR, Kant Chemical Co.,Ltd). Subsequently, these samples were further ultrasonically washed with acetone, anhydrous ethanol and deionized water followed by air drying. Accordingly, the fresh titanium sheet was named as P–Ti in this research.

### 2.2. Fabrication of nano-texture

Then, the fresh titanium sheet with an exposed area of 1 cm$^2$ was set as an anode for twice electrochemical anodization. In which, the graphite sheet was applied as a cathode, the electrolyte consisted of 0.5 *wt*% ammonium fluoride (NH$_4$F, AR, Tianjin Damao Chemical Reagent Co.Ltd), 2 *vol*% deionized water and ethylene glycol (C$_2$H$_6$O$_2$, AR, Tianjin Fuyu Chemical Co.Ltd) in the first anodization treatment. This anodic oxidation reaction was performed with a DC regulated power supply (MS1003DS, Maisheng Powere Technology Co.Ltd, China) at a constant potential 50 V for 1 h. After the nanotube generated on the titanium sheet surface by the first anodization, the titanium sheet was put out and placed into an ultrasonic water bath device for peeling the ordered nanotube layer shown in Fig. 2(a1-a3). Subsequently, the sample was again adopted as an anode and anodized in 5 *wt*% phosphoric acid (H$_3$PO$_4$, 85 %, Macklin) electrolytes at potential 50 V for 3 min. After the second anodization, the regular nanotexture was prepared on the titanium sheet surface shown in Fig. 2(a4). Accordingly, the sample with nanotexture was named as N–Ti. To separately explore the effect of nanostructure on cells adhesion, fresh titanium sheet was adopted as an anode and anodized only in 5 *wt*% H$_3$PO$_4$ electrolytes at potential 50 V for 3 min, the sample was named as F–Ti, which was shown in Fig. 2(a1) and (b1).
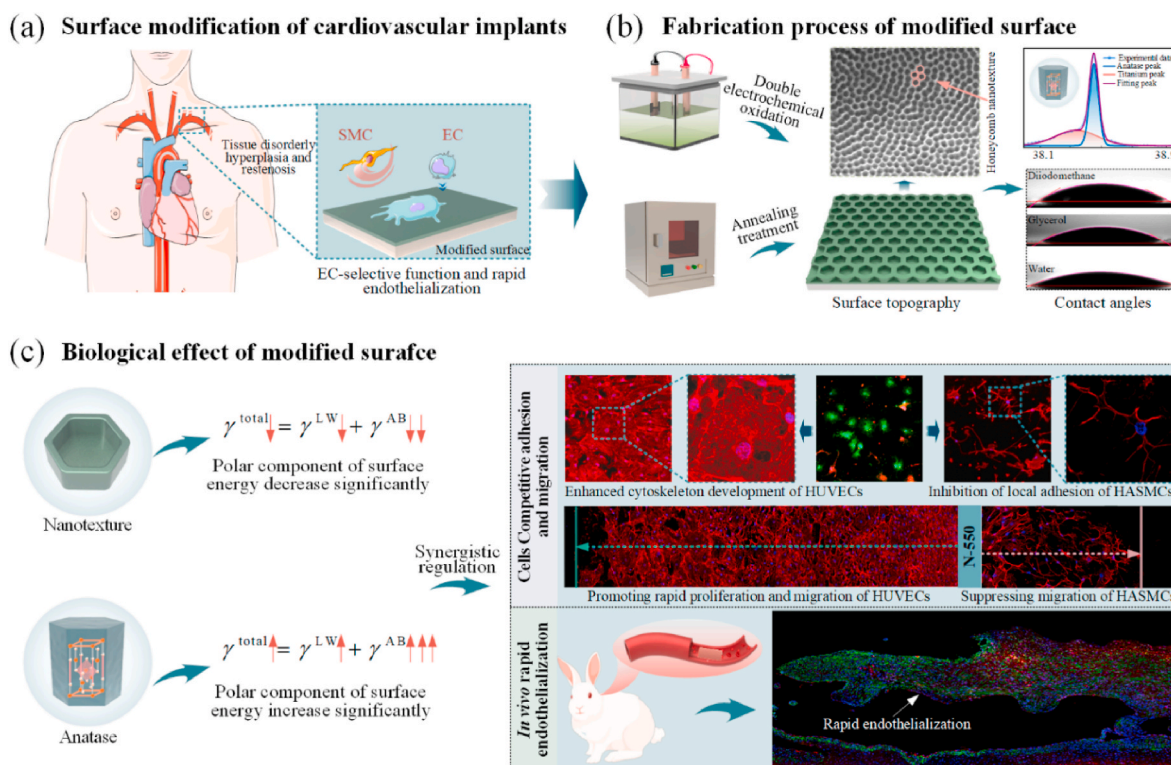
**Fig. 1.** EC-selective modified strategy. **(a)** Nanotexture and crystal phase-derived surface properties for EC-selective cells adhesion and rapid endothelialization to address the clinical problem of tissue disorderly hyperplasia on the vascular implant/interventional devices surfaces; **(b)** Fabrication process and physicochemical properties of the modified surface; **(c)** Biological effect of vascular tissue cells adhesion and proliferation regulated by nanotexture and crystal phase on the modified surface.

### 2.3. Heat treatment for crystal phase regulation

Annealing treatment, as a common heat treatment process, is usually adopted to regulate the physicochemical properties such as crystalline structure and grain size. To obtain different $TiO_2$ crystal phase, the N–Ti and F–Ti were respectively annealed in air at 550 °C, 900 °C for 3 h using a muffle furnace (KSL-1200X, Hefei Kejing Material Technology Co., Ltd, China), where the heat rate is 15 °C/min. Finally, the annealed N–Ti and F–Ti samples were named as N-550, N-900, F-550, and F-900, respectively.

### 2.4. Surface characterization

The surface morphology of different samples was characterized using scanning electron microscope (Quanta FEG250, SEM, USA). Based on the SEM images, the structural parameters of honeycomb nanotexture annealed under different temperatures were quantitively analyzed with the help of ImageJ software. The crystal phase was detected by X-ray diffraction (Bruker D8 Advance, XRD, Germany) with an incident Cu $K_\alpha$ radiation ($\lambda = 0.154$ nm). Additionally, the static water contact angle of different samples (n = 3) was measured with an optical contact angle system (CAM101, KSV, Finland). Meanwhile, the contact angles of polar liquids (glycerol ($C_3H_8O_3$, AR, Tianjin Fuyu Chemical Co.Ltd)) and apolar liquids (diiodomethane ($CH_2I_2$, AR, Energy Chemical Co.Ltd)) on the different sample surfaces were also measured, which were adopted to characterize and calculate the surface tension component of all samples. Each experimental group has three individual separate samples to ensure the reliability of the measurement result.

### 2.5. Cells attachment and proliferation on modified surfaces

Human vascular endothelial cells (HUVECs) and human aortic smooth muscle cells (HASMCs) was selected to analyze the synergistic regulation mechanism of vascular tissue cells adhesion and proliferation affected by crystal phase and nanotexture of $TiO_2$-based biomaterials. First, all samples were sterilized by using 75 % alcohol solution. HUVECs and HASMCs were seeded on each sample surface at a concentration of $1.5 \times 10^4$ cells/mL and $2 \times 10^4$ cells/mL, respectively. Subsequently, they were cultured in humidified air containing 5 % $CO_2$ at 37 °C for 24 h, 48 h, and 72 h, respectively. After each predetermined time out, the sample was put out and cells adhered on the surface were fixed with 4 % paraformaldehyde. Then, the TRITC-phalloidin (Solarbio, CA1610) was used to stain the filamentous actin (F-actin) which is one of the components of cell cytoskeleton and closely related to cytoskeleton rearrangement and motility of cells. Hoechst 33342 (Solarbio, C0031) was used to stain the nuclei of the adherent cells. After completion, the proliferation behaviors of HUVECs and HASMCs were observed by laser confocal microscope (LSM900, Zeiss, Germany). Cells proliferation was quantitively analyzed by calculating the density and spreading area of cells adhered on the materials surface. In this case, each experimental group has three individual separate samples, three pictures taken from each sample surface were applied to count the number of cells and spreading area.

### 2.6. Analysis of CD31 and VE-cadherin expression in HUVECs

CD31 and VE-Cadherin expression were detected to assess the quality of endothelium. HUVECs were seeded at a concentration of $1 \times 10^4$ cells/mL, and then were cultured in fresh medium for 48 h. After incubation, CD31 and VE-Cadherin of HUVECs were stained by using mouse anti-CD31 antibody (Bioss, BH0190) and rabbit anti- VE-Cadherin as the primary antibody, respectively. Then, Alexa Fluor 594 goat anti-mouse IgG (Boiss, bs-0296G-AF594) and Alexa Fluor 488 goat anti-rabbit IgG (Boiss, bs-0295G-AF488) were used as the secondary
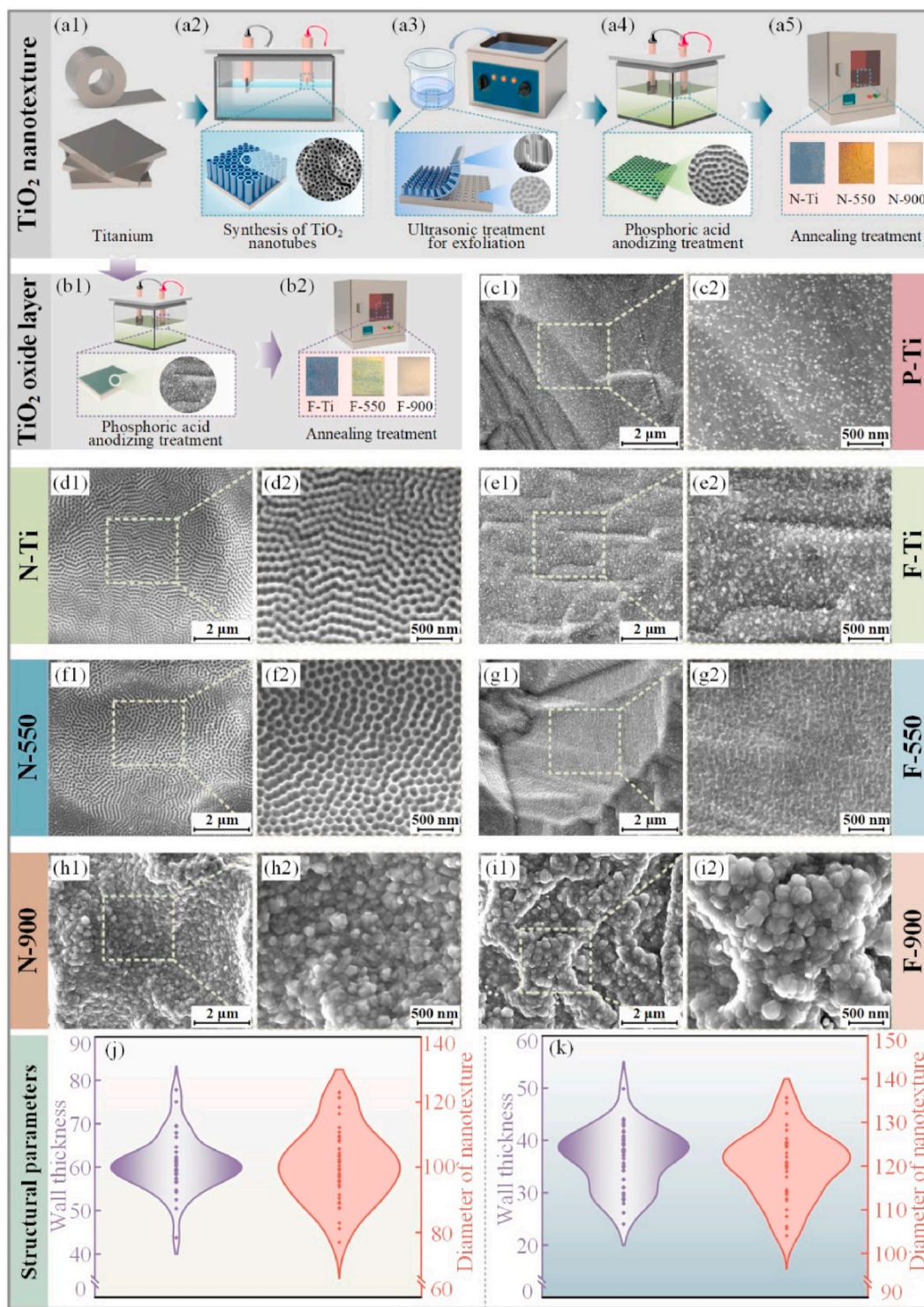
**Fig. 2.** Fabrication process and surface morphology of different samples. **(a1-a5)** Fabrication process of the sample with honeycomb nanotexture; **(b1-b2)** Fabrication process of the samples with TiO₂ oxide layer; **(c1-c2)** Original pure titanium surface (P–Ti); **(d1-d2)** Surface morphology of unannealed honeycomb nanotexture (N–Ti); **(e1-e2)** Surface morphology of unannealed oxide layer (F–Ti); **(f1-f2)** Surface morphology of honeycomb nanotexture annealed at 550 °C (N-550); **(g1-g2)** Surface morphology of oxide layer annealed at 550 °C (F-550); **(h1-h2)** Surface morphology of honeycomb nanotexture annealed at 900 °C (N-900); **(i1-i2)** Surface morphology of oxide layer annealed at 900 °C (F-900); **(j)** Wall thickness and diameter of honeycomb nanotexture without annealing treatment; **(k)** Wall thickness and diameter of honeycomb nanotexture annealed at 550 °C.

antibody. Additionally, cell nuclei of HUVECs were counterstained with Hoechst 33342. Finally, the CD31 and VE-Cadherin expression in single HUVEC was observed by laser scanning confocal microscopy. Similarly, each experimental group has three individual separate samples, three fluorescence pictures were taken from each sample surface. To ensure the accuracy of the fluorescence intensity measured from single cell and the validity of data in the statistical analysis, some cells with clear and integral boundaries were selected from multiple immunofluorescence images to measure the fluorescence intensity using ImageJ software.

## 2.7. Cells migration behaviors on modified surfaces

Enhanced migration of HUVECs and suppression of HASMCs are vital for *in situ* regeneration of a healthy endothelial layer on the surfaces of blood-contacting vascular implants. In this work, the migration test was performed to further reveal the endothelialization potential of modified surfaces with different crystal phase and nanotexture. In brief, a 12 mm × 3 mm specimen sheet was vertically folded in half, then one half of the specimen was immersed into the cells suspension to obtain a confluent cells layer on the surface. After incubation for 12 h, the specimen was taken out and vertically turned over before placed into a new plate, then fresh culture medium was added. After incubation for 72 h, the specimen sheet was cut along the crease line and cells adhered on the surface was stained according to the staining processed described above. HUVECs and HASMCs migration ability on different modified surfaces was evaluated by measuring the distance from the most distal migrating cells to the crease line. Among them, each experimental group has three individual separate samples, and the migration behavior and distance of cells on each sample surface were recorded for each group.

## 2.8. Co-culture of HUVECs and HASMCs on modified surfaces

In the co-culture experiment, HUVECs and HASMCs were mixed at a ratio of 1:1 with a final concentration of $2 \times 10^4$ cells/mL. Subsequently, they were seeded on the sample surfaces and co-cultured for 7 days in a mixed medium consisting of 50 % Endothelial Cell Medium (ECM, Sciencell, Cat. No 1001) and 50 % Smooth Muscle Cell Medium (SMCM, Sciencell, Cat. No 1101), in which the culture medium was replaced every 24 h. After the predetermined time point, the samples were taken out and adherent cells were fixed with 4 % paraformaldehyde. To further analyze the competitive growth behavior between HUVECs and HASMCs and evaluate the integrity and maturity of cells co-cultured on different sample surfaces, the proteins expression of CD31 in HUVECs and α-SMA in HASMCs were detected by immunofluorescence staining. CD31and α-SMA was stained with mouse anti-CD31 antibody (Bioss, BH0190) and rabbit anti-α-SMA (Bioss, bs-10196R) as the primary antibody, respectively. Then, Alexa Fluor 594 goat anti-mouse IgG (Boiss, bs-0296G-AF594) and Alexa Fluor 488 goat anti-rabbit IgG (Boiss, bs-0295G-AF488) were used as the secondary antibody. Additionally, cell nuclei of HUVECs and HASMCs were counterstained with Hoechst 33342. Finally, the CD31 and α-SMA expression was observed by laser scanning confocal microscopy. From there, it was also further observed whether the endothelial cells could proliferate massively to cover the smooth muscle cells after long-term co-culture thereby assessing the pro-endothelialization performance of the modified surfaces. Similarly, each experimental group has three individual separate samples, and the proliferation behaviors of cells on each sample surface were recorded for each group.

## 2.9. In vivo animal test

The lamellar samples were rolled into tube implants with small diameter (sizes of tube implant: approximately 1.1 mm inner diameter, 7 mm length and 0.1 mm thickness), followed by seam-sealing with jewelry welding. After that, the tube implants were implanted into the left carotid artery of rabbit. Briefly, New Zealand rabbits weighting 2.5–3.0 kg were selected as experimental animals (the number of animals in the control and experimental groups was three, respectively.), and all rabbits were fed under the same experimental conditions, and anesthetized by inhalation anesthetics. After being completely unconscious, the rabbit hair around the neck was removed with depilatory cream and the skin surface was disinfected using iodophor, followed by a skin incision to expose the left internal carotid artery. The proximal and distal ends of the vessel are clamped with two vascular clips, an incision of approximately 3–5 mm length is made in the clamped carotid artery region. The prepared tube implant is then immediately placed

into the vessel and the vascular incision is closed with a 6–0 prolene suture. After confirming that there was no bleeding from the vascular incision when the clip was removed, the soft tissue and skin were closed sequentially and the wound was finally disinfected. To exclude the influence of anticoagulants on the evaluation of antithrombotic performance of implant surface, experimental rabbits were not given any anticoagulants after surgery. Each rabbit was only injected intramuscularly with enrofloxacin (0.5 mL/10 kg) twice a day for one week to prevent wound infection. Whole experimental procedure complied with the Animal Ethics Committee of Shandong University (Approval No. ECSBMSSDU2020-2-059).

One month after implantation of the tube implant, the experimental rabbit was reoperated and the neck skin was incised to expose the left internal carotid artery. A section of vascular tissue wrapping the tube implant was intercepted for the histological analysis. Specifically, as shown in Fig. S1, the vascular tissue wrapping the tube implant was dissected along the axial direction, and the profile of vascular tissue was stained to observed the tissue proliferation and inflammatory response. Meanwhile, as shown in Fig. S2, the hyperplasia tissue generated in the lumens of tube implant was also stained for histological analysis to further evaluate endothelial regeneration on the surface of tube implant. Firstly, the vascular tissue was fixed, dehydrated, and embedded in paraffin. Then the tissue was respectively stained with Hematoxylin - eosin (HE) and Masson's trichrome to analyze the inflammatory response and re-endothelialization behavior. Additionally, the immunofluorescent staining was performed to further observed endothelial regeneration. Endothelial cells grew in the vascular tissue wrapping the tube implant were stained with rabbit anti-CD31 antibody (Bioss, bs-0195R), and smooth muscle cells were also stained with rabbit anti-alpha smooth muscle actin (anti-α-SMA) antibody (Bioss, bs-10196R). After that, Alexa Fluor 594 goat anti-rabbit IgG (Boiss, bs-0295G-AF594) and Alexa Fluor 488 goat anti-rabbit IgG (Boiss, bs-0295G-AF488) as the secondary antibody, respectively. Lastly, the stained tissue was observed by laser confocal microscope.

## 2.10. Statistical analysis

All experiments were repeated with three individual separate samples in each group. Experimental data was presented as mean ± standard deviation. To ensure the validity of the statistical analysis, all data was previously checked for normality test and homogeneity of variance test. Subsequently, statistical analysis was performed using one-way analysis of variance (ANOVA) followed by Tukey's post hoc test with the Origin software. A $p$ value less than 0.05 was considered statistically significant.

## 3. Results and discussion

### 3.1. Surface topography and microstructure of modified surfaces

Honeycomb nanotexture was fabricated as described in Fig. 2(a1-a5), as illustrated in Fig. 2(c1-c2), the original titanium surface exposed clear grain boundaries after ultrasonic acid etching. Highly organized honeycomb nanostructure formed on the titanium surface shown in Fig. 2(d1-d2). Subsequently, the surface morphology of honeycomb nanotexture presented slight change when the annealing temperature is at 550 °C. Specifically, the nanotexture suffered a slight dissolution and wall thickness observed from the micrography became thinner shown in Fig. 2(f1) and (f2). Based on the SEM images, the structural parameters including the diameter and wall thickness of individual honeycomb nanopore were measured and analyzed with the help of ImageJ software. Specifically, the individual data point in Fig. 2(j) and (k) referred to the structural data of each nanopore. Statistical analysis showed that the diameter and wall thickness of the unannealed honeycomb nanopore was approximately $100 \pm 11$ nm and $60 \pm 6$ nm. However, the diameter of the honeycomb nanopore increased to $120 \pm 7$ nm and the wall

thickness decreased to 36 ± 5 nm after the annealing treatment at 550 °C. By contrast, as the annealing temperature increased to 900 °C, the regular nanotexture completely disappeared leaving small and dense grains with irregular shapes. According to the XRD spectra shown in Fig. 3(a), besides some diffraction peaks corresponding to titanium, many additional diffraction peaks corresponding to rutile phase were observed in the XRD spectra, which indicated that only rutile generated in the samples N-900 and F-900. Due to the difference in the lattice constants between the anatase and rutile, the crystal phase transformation from anatase to rutile would induce volume contraction (approximately 8 %) [39,40], which was reflected by the collapsed of regular nanotexture and the formation of fine rutile grains shown in Fig. 2(h1-i2). Meanwhile, to comparative analyze the effect of nanotexture on modified surface performance while excluding the interference of chemical composition, the TiO₂ oxide layer was prepared on the titanium surface as presented in Fig. 2(b1-b2). As shown in Fig. 2(e1-e2) and (g1-g2), the surface morphology of samples did not show significant difference compared to the original titanium surface whether they were annealed at 550 °C or not. However, the previously formed flat oxide layer also completely disappeared at 900 °C. Similar to N-900, a large number of fine grains generated spontaneously, disorderly stacking to form particles with varying sizes as shown in Fig. 2(i1-i2).

### 3.2. Analysis of crystal phase transformation

Annealing treatment can effectively regulate the crystal structure (e. g., crystal phase type, grain size and shape) of materials, which is widely applied to improve the physicochemical properties of materials. Crystal phase of modified layer in all samples were characterized by XRD shown in Fig. 3. Only some peaks corresponding to Ti were detected for origin titanium surface (P–Ti), un-annealed nanotexture surface (N–Ti), and un-annealed oxide layer surface (F–Ti), indicating that the crystal phase in the modified layer of N–Ti and F–Ti were amorphous. At the

annealing temperature of 550 °C, some additional diffraction peaks corresponding to anatase presented in the XRD spectra of N-550 and F-550 shown in Fig. 3(b1-b2) and (c1-c2), which manifested that annealing treatment induced the transformation of crystal phase from amorphous to anatase. Thus, the reorganization and growth of the crystal structure resulted in a slight change in the surface topography of nanotexture (N-550) compared with N–Ti. Furthermore, annealing treatment at higher temperature 900 °C favored the formation of rutile phase, resulting in only rutile generated in the surface of N-900 and F-900. According to previous research [41], due to the difference of lattice constants between the anatase and rutile, the crystal phase transformation from anatase to rutile would induce volume contraction (approximately 8 %), which is reflected by the collapsed of regular nanotexture and the formation of fine rutile grains shown in Fig. 2 (h1-i2). As stated by Huang et al. [42,43], the collapse of regular nanotexture could be traced to growth of rutile at the interface between the barrier layer (an electrically insulating layer separating nanotexture from contacting titanium) and titanium substrate in which the metal is thermally anodized.

### 3.3. Wettability characterization and surface energy calculation

Surface wettability plays an important role in regulating biological effect of material surface. Typically, the wettability is characterized by the contact angle of water droplets on the material surface. As shown in Fig. 4, the contact angle of water droplets reflected an enhancement in the hydrophilicity of the sample surface as the annealing temperature increased. Furthermore, to quantitatively analyze the wettability, the surface energy components (apolar component and polar component) of different sample surfaces were calculated based on the complete Young-equation. For the condensed phase materials, the surface tension $\gamma^{total}$ of sample consists of two components which are apolar component ($\gamma^{LW}$) induced by van der Waals force and polar component ($\gamma^{AB}$) induced by
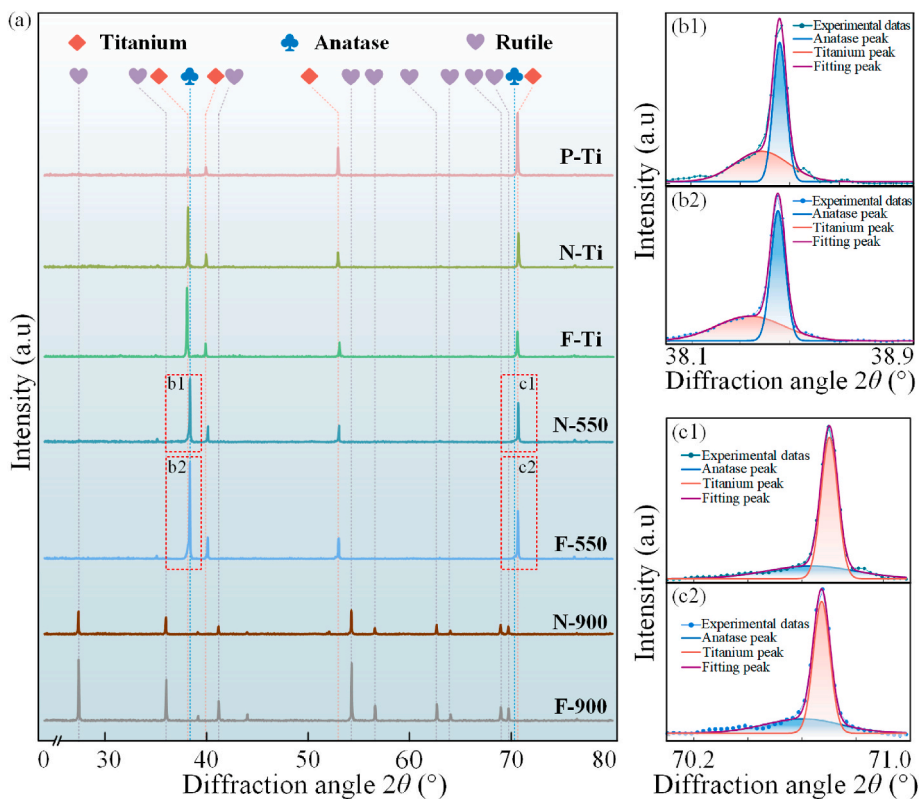


**Fig. 3.** Detection of crystal phase on the surface of all samples. **(a)** XRD spectra of all samples; **(b1-b2)** Detailed analysis of XRD spectra located at 38.1°–38.9° of nanotexture and oxide layer annealed at 550 °C (N-550 and F-550); **(c1-c2)** Detailed analysis of XRD spectra located at 70.2°–71° of N-550 and F-550.
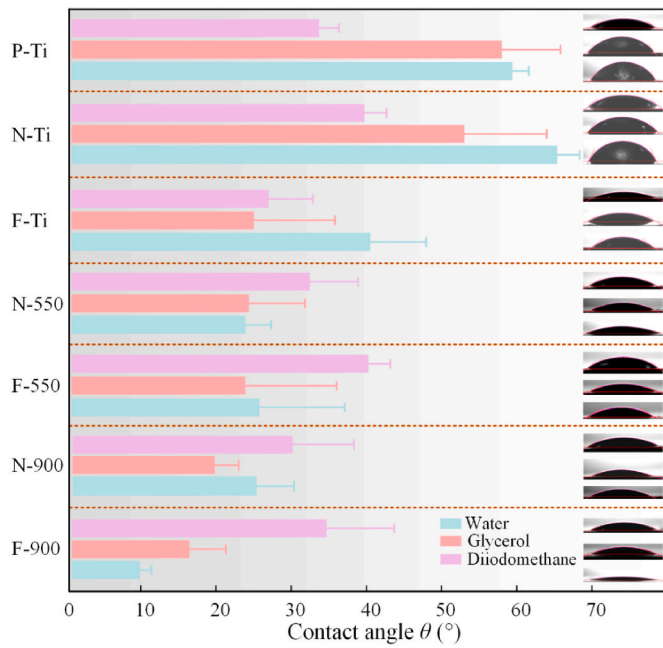
**Fig. 4.** Contact angles of water, glycerol, and diiodomethane droplets on different samples surfaces. Original pure titanium (P–Ti), un-annealed nano-texture (N–Ti); un-annealed oxide layer (F–Ti), nanotexture annealed at 550 °C (N-550), oxide layer annealed at 550 °C (F-550), nanotexture annealed at 900 °C (N-900), oxide layer annealed at 900 °C (F-900).

Lewis acid-base force [44], which can be expressed as

$$\gamma^{\text{total}} = \gamma^{\text{LW}} + \gamma^{\text{AB}} \tag{1}$$

where $\gamma^{\text{LW}}$ and $\gamma^{\text{AB}}$ respectively denote apolar component and polar component of surface tension [45]. Additionally, according to Young--Dupré equation that is the best described as a force-balance equilibrium [46], we can get that the following equation

$$(1 + \cos\theta)\gamma_{\text{L}}^{\text{total}} = -\Delta G_{\text{SL}} \tag{2}$$

where $\theta$ is the contact angle of liquid on the solid surface, $\gamma_{\text{L}}^{\text{total}}$ is the total surface tension of liquid, $\Delta G_{\text{SL}}$ denotes the interaction energy between the solid phase and liquid phase. At the same time, by using Dupré equation [47], $\Delta G_{\text{SL}}$ can be obtained as follows

$$\Delta G_{\text{SL}} = -2\left(\sqrt{\gamma_{\text{S}}^{\text{LW}}\gamma_{\text{L}}^{\text{LW}}} + \sqrt{\gamma_{\text{S}}^{+}\gamma_{\text{L}}^{-}} + \sqrt{\gamma_{\text{S}}^{-}\gamma_{\text{L}}^{+}}\right) \tag{3}$$

In Eq. (3), the footnotes S and L respectively denote solid phase and liquid phase. In addition, the polar component of surface tension $\gamma^{\text{AB}}$, contains two non-additive parameters, which are the electron-acceptor surface tension parameter named as $\gamma^{+}$ and the electron-donor parameter named as $\gamma^{-}$, which can be shown as

$$\gamma^{\text{AB}} = 2\sqrt{\gamma^{+}\gamma^{-}} \tag{4}$$

combining Eq. (2) and Eq. (3), the complete Young-equation can be expressed as

$$(1 + \cos\theta)\gamma_{\text{L}}^{\text{total}} = 2\left(\sqrt{\gamma_{\text{S}}^{\text{LW}}\gamma_{\text{L}}^{\text{LW}}} + \sqrt{\gamma_{\text{S}}^{+}\gamma_{\text{L}}^{-}} + \sqrt{\gamma_{\text{S}}^{-}\gamma_{\text{L}}^{+}}\right) \tag{5}$$

According to Eq. (5), the $\gamma_{\text{S}}^{\text{LW}}$, $\gamma_{\text{S}}^{+}$, and $\gamma_{\text{S}}^{-}$ of all samples can be obtained by measuring the contact angle $\theta$ of three kinds of liquids with known surface tension on the sample surfaces.

As shown in Fig. 4 and Table 1, the polar liquids (water and glycerol) and apolar liquids (diiodomethane) were adopted to characterize and calculate the surface tension component of all samples. Based on Eq. (5),

**Table 1**
Surface tension properties of all samples.

| Materials | $\gamma^{\text{total}}$ (mN/m) | $\gamma^{\text{LW}}$ (mN/m) | $\gamma^{\text{AB}}$ (mN/m) | $\gamma^{+}$ (mN/m) | $\gamma^{-}$ (mN/m) |
|---|---|---|---|---|---|
| Water | 72.80 | 21.80 | 51.00 | 25.50 | 25.50 |
| Glycerol | 64.00 | 34.00 | 30.00 | 3.92 | 57.40 |
| Diiodomethane | 50.80 | 50.80 | 0 | 0 | 0 |
| P–Ti | 53.46 | 42.88 | 10.58 | 2.59 | 10.80 |
| N–Ti | 46.72 | 40.12 | 6.60 | 0.89 | 12.24 |
| F–Ti | 61.29 | 45.69 | 15.60 | 2.52 | 24.14 |
| N-550 | 60.59 | 43.48 | 17.11 | 1.68 | 43.56 |
| F-550 | 60.05 | 39.86 | 20.19 | 2.57 | 39.64 |
| N-900 | 62.71 | 44.53 | 18.18 | 2.21 | 37.39 |
| F-900 | 62.85 | 42.54 | 20.31 | 2.23 | 46.26 |

$\gamma_{\text{S}}^{\text{LW}}$, $\gamma_{\text{S}}^{+}$, and $\gamma_{\text{S}}^{-}$ of all samples were obtained shown in Table 1. The surface tension of original titanium surface was 53.46 mN/m. Combining Table 1 and Fig. 4, it could be observed that nanotexture generated on the titanium surface without annealing treatment (N–Ti) induced a slight decrease in the surface tension compared to pure titanium surface (P–Ti), which could be attributed to the difference in composition and micromorphology, i.e., the nanotexture layer covering titanium surface was composed of amorphous TiO$_2$. Additionally, a pinning effect induced by regular semi-closed nanotexture hindered the liquid infiltration, thus resulting in a lager liquid contact angle compared to flat titanium surface [48]. When the samples were annealed at 550 °C, whether the surfaces were with nanotexture (N-550) or without nanotexture (F-550), the surface tension increased to about 60 mN/m compared to P–Ti, and the polar component increased significantly. The phenomenon was mainly associated with the generation of anatase with high surface energy in the oxidized layer shown in Fig. 3. As shown in Fig. 4, the remarkable decrease in the liquids contact angles on the surfaces of N-550 and F-550 could intuitively reflected an increase of surface energy. Upon annealing temperature up to 900 °C, rutile with higher surface energy nucleated at the interface of anatase grains due to the increase in thermal vibrational energy of Ti and O atoms [43]. With the increase in annealing time, many fine rutile grain generated shown in Fig. 2(h1-i2). On the nanoscale, surface area per unit volume would increase due to the grain refinement and increased grain boundary, accompanied with higher surface energy. Through a series of comparative analysis, it was found that the nanotexture and crystal phase can effectively regulate the surface energy of material, thus inducing change in its apparent wettability.

### 3.4. Attachment and proliferation behaviors of HUVECs and HASMCs

For bare metal implants, TiO$_2$ is widely considered as one of the most promising inorganic coatings [28], with alteration in its surface chemistry, crystalline phase and topography contributing to improved biocompatibility. Therefore, the effect of surface topography and crystal phase of TiO$_2$-based biomaterials on vascular tissue cells adhesion and proliferation were analyzed by characterizing the adhesion and proliferation behaviors of HUVECs and HASMCs on different sample surfaces.

The preliminary discussion about adhesion and proliferation behaviors of cells was performed by observing the immunofluorescence images. As shown in Fig. 5(a1-g3), red color denoted filamentous actin which was characterized to analyze cytoskeleton development and evaluate the cells attachment behaviors on different sample surfaces. First, the fluorescence micrographs showed that individual HUVEC grown on the surfaces of N–Ti, N-550, and F-550 displayed a larger spreading morphology compared with other groups, and when the incubation time was prolonged to 48 h, these sample surfaces were fully covered by the HUVECs showing a tight fusion with each other. However, compared with the above experimental groups, the surfaces of P–Ti and F–Ti were not completely covered by cells until the incubation time was extended to 72 h, implying a decrease in the cell proliferation rate.
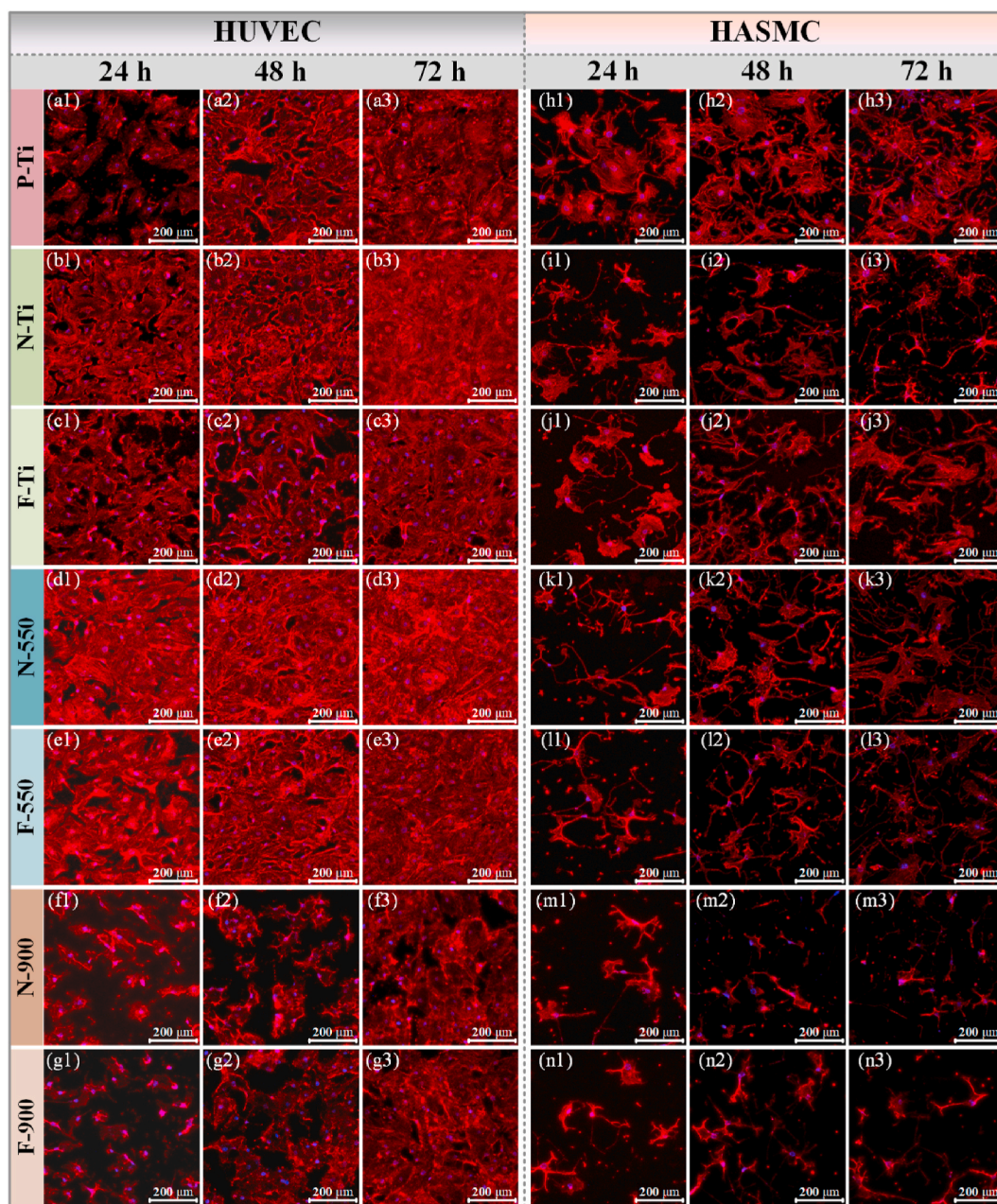
**Fig. 5.** Immunofluorescence staining micrographs of HUVECs and HASMCs after being cultured for 24 h, 48 h, and 72 h on different sample surfaces. **(a1-g3)** HUVECs respectively adhered on original pure titanium surface (P–Ti), un-annealed nanotexture surface (N–Ti); un-annealed oxide layer surface (F–Ti), nanotexture surface annealed at 550 °C (N-550), oxide layer surface annealed at 550 °C (F-550), nanotexture surface annealed at 900 °C (N-900), oxide layer surface annealed at 900 °C (F-900); **(h1-n3)** HASMCs respectively adhered on the surfaces of P–Ti, N–Ti, F–Ti, N-550, F-550, N-900, and F-900. (Blue color denoted nucleus, red color denoted filamentous actin). (For interpretation of the references to color in this figure legend, the reader is referred to the Web version of this article.)

Additionally, HUVECs showed an inactive morphology on the surfaces of N-900 and F-900, and the sample surfaces were still not completely covered after 72 h, suggesting an extremely slow proliferation rate. Besides the biological behavior of HUVECs, which is relevant for tissue hyperplasia and thrombosis on the surfaces of blood-contacting medical devices, the adhesion and hyperproliferative behavior of HASMCs is major factor affecting its occurrence. As shown in Fig. 5(h1-n3), HASMCs mainly exhibited disorderly extension morphology, accompanied by longer tentacles. Preliminarily, the proliferation pattern of HASMCs on different samples surfaces were not consistent with those of HUVECs. Among them, the proliferation rate of HASMCs on the F–Ti surface showed no significant difference compared with that of P–Ti due to possessing the same crystal phase and surface topography, and it was

also the fastest compared with other groups. Additionally, the proliferation rate of HASMCs on the surfaces of N-900 and F-900 was the slowest, which indicated that N-900 and F-900 not only inhibited the adhesion and proliferation of HUVECs, but also limited the growth of HASMCs. Initially, it could be found that the surface topography and crystal phase of $TiO_2$-based materials have a significant effect on the proliferation behaviors of HUVECs and HASMCs. To deeply discuss the effect of modified surface properties on the proliferation behaviors of cells, the number and single-cell spreading area of HUVECs and HASMCs were quantitatively and statistically analyzed in the next section.

Cells grew on the foreign material usually from following a series of developmental process such as substrate attachment, cell spreading, and cytoskeleton development [49]. Fig. 6 presented the fluorescence
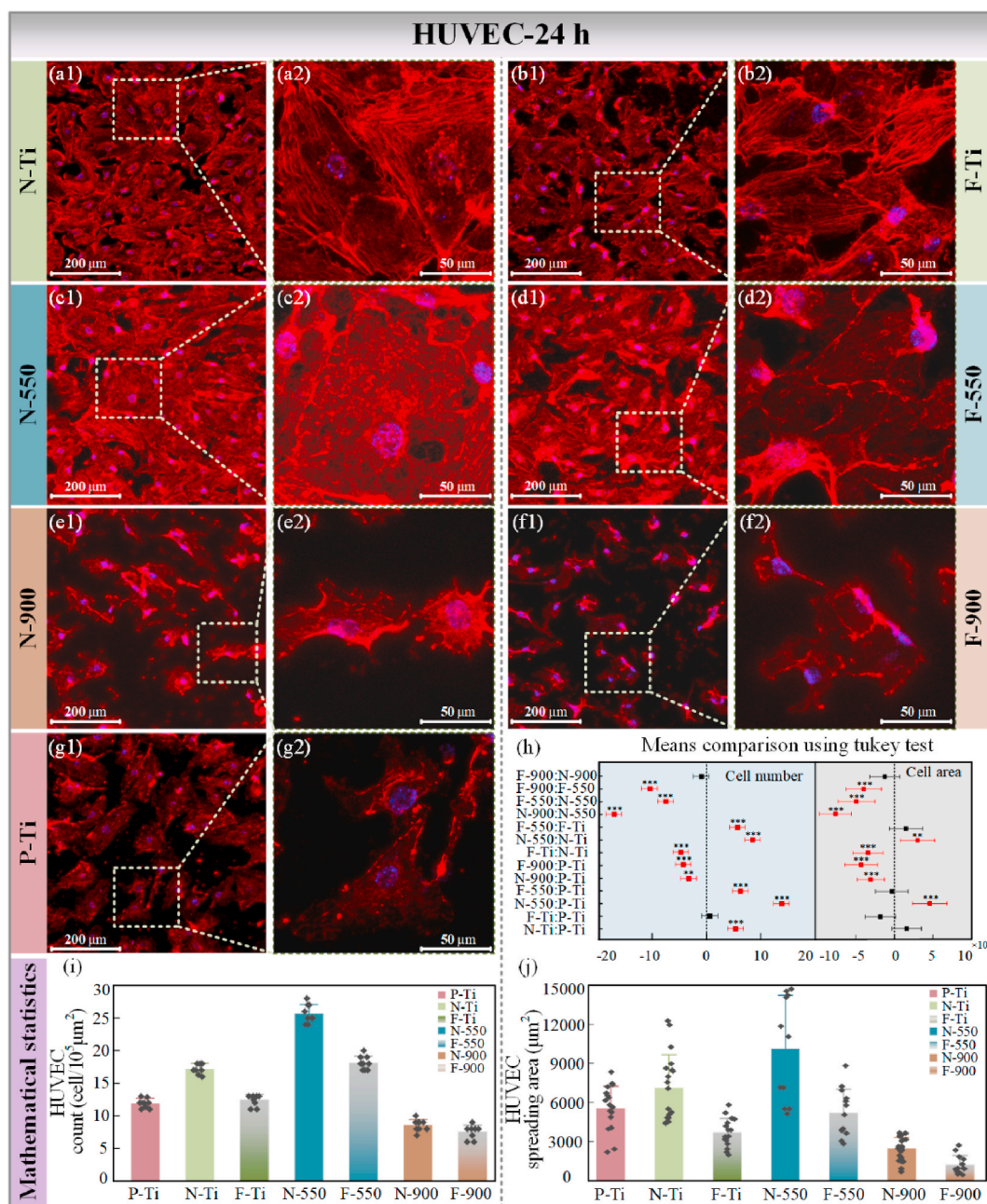
**Fig. 6.** Cytoskeletal actin stains and statistical analysis of HUVECs cultured on different samples surfaces for 24 h. **(a1-g2)** Fluorescent images of HUVECs attached on different sample surfaces; **(h)** Statistical analysis of adhered number and spreading area of HUVECs using one-way analysis of variance (ANOVA) followed by Tukey's post hoc test, *$P < 0.05$, * *$P < 0.01$, ***$P < 0.001$; **(i)** Amounts of HUVECs attached on the different samples surfaces; **(j)** Single-cell spreading area of HUVECs on different sample surfaces (blue color denoted nucleus, red color denoted filamentous actin). (For interpretation of the references to color in this figure legend, the reader is referred to the Web version of this article.)

microscopic image and statistical results of HUVECs cultured on different sample surfaces for 24 h. First, red color denoted filamentous actin which was stained by TRITC-phalloidin to analyze cytoskeleton development and evaluate the cells attachment behaviors of cells. As shown in Fig. 6(a1-g2), much more pronounced filamentous extension and lager spreading area of each cell was observed on the N-550 surface, accompanied with a fully developed cytoskeleton, which indicated that the N-550 surface provided a better microenvironment for attachment and spreading of HUVECs compared with other samples. In contrast, HUVECs attached on the surfaces of N-900 and F-900 exhibited small and rounded morphology without obvious pseudopod extensions, implicating a slower proliferation rate.

Subsequently, the statistical analysis revealed that nanotexture

significantly promoted cell spreading by a comparison between the groups of N–Ti and F–Ti. According to the statistical results of cells adhered on the F-550, it could be found that the presence of anatase did not produce significant effect on both cells attachment and morphology compared to the F–Ti. However, the comparison of cells growth states on the surfaces of N-550 and N–Ti, N-550 and F-550 showed that the combination of regular nanotexture and anatase greatly promoted the attachment and spreading of HUVECs. As presented in Fig. 6(i) and (j), the number of HUVECs adhered to the surface of N-550 was maximum and they had the largest cell spreading area. Some studies have confirmed that highly ordered features, such as TiO$_2$ nanotube, can result in an enhancement in HUVECs motility and proliferation [50]. As shown in Fig. 2(d2) and (f2), highly organized honeycomb

nanostructure was formed on the surfaces of N–Ti and N-550, which provided a suitable nano-topography for promoting HUVECs growth. In addition, as the annealing treatment increased to 900 °C, the regular nanotexture completely disappeared generating many small and dense rutile grains with irregular shapes. As a result, the attachment and cytoskeleton development were significantly suppressed along with the disappearance of the nanotexture and generation of rutile. Specifically, the comparative analysis of F-900 and F-550 revealed that rutile phase resulted in a substantial weakness in cells proliferation, and the cells growth state on the surfaces of N-900 and N-550 further confirmed that the collapse of nanotexture and formation of rutile did not provide a suitable microenvironment for cells attachment, spreading, and cytoskeleton development.

To further examine the integrity and maturity of endothelial cells cultured on different sample surfaces, the expression of CD31 (platelet endothelial cell adhesion molecule) in HUVECs cultured in ECM with different samples was analyzed by immunofluorescence staining. As shown in Fig. 7(a2-a5), the presence of nanostructures significantly elevated the spreading of the endothelial cell skeleton as well as the expression of CD31, suggesting a high cell maturation by comparing the fluorescence results of the two groups, N–Ti and F–Ti, N-550 and F-550. Additionally, a further scrutinization delineated an intensified expression of CD31 within HUVECs cultured on the nanotexture surface annealed at 550 °C (N-550), demonstrating that the transition from amorphous to anatase phase of $TiO_2$ promoted the formation of confluent and compact endothelial monolayer. Overall, distinct increase in CD31 expression were observed in the HUVECs attached on the surface of N-550 than other samples, reaffirming the ability of nanostructure and crystal phase offered a positive effect on endothelial maturation. Meanwhile, expression of the junction protein VE-Cadherin was further examined to confirm the integrity of the regenerated cell monolayer. As shown in Fig. 7(d1-f7), HUVECs cultured on the surface of N-550 was visually integrated well with the neighboring cells, a close look into the cell-cell junction indicated cell-cell junctions became thicker, forming a more stable reticular morphology after the combination between nanostructure and anatase on the titanium surface, while significant decline in expression of VE-Cadherin was observed when the annealing treatment temperature of samples increased to 900 °C, which mainly attributed to the disappearance of nanostructure and anatase. The immunofluorescent results showed that either nanostructure or anatase phase upregulated the expression of VE-Cadherin and promoted cell-cell interaction for HUVECs monolayer integrity.

In the early stage of vascular implantation, an anti-proliferative performance against smooth muscle cells is crucial to inhibit tissue disorder proliferation such as in-stent stenosis. Therefore, more details about proliferation behavior of HASMCs on different sample surfaces needed to be discussed. Fig. 8(a1-g2) presented the typical fluorescence microscopic images of cytoskeleton arrangement in the HASMCs cultured on different samples surface for 24 h. First, HASMCs attached on the pure titanium surface presented a fully spreading cell morphology with a large cell size than that attached on other sample surfaces, indicating an active cells growth state. The statistical results of adhered number and single-cell spreading area revealed that the pure titanium surface favored the rapid proliferation of HASMCs, which also confirmed that the bare titanium implant surface still faced a high risk of tissue proliferation. Subsequently, a comparative analysis of cell morphology on the surfaces of N–Ti and P–Ti revealed that the existence of nanotexture led to a decrease in the number and spreading area of adherent HASMCs. As shown in Fig. 8(a2), HASMCs adhered to the N–Ti surface through localized adhesion sites generated by multiple circular pseudopodia, indicating a potential local adhesion behavior compared to the fully spreading morphology on the pure titanium surface. Furthermore, at annealing temperature of 550 °C, the introduction of anatase induced a decrease in the HASMCs attachment by statistically analyzing the number of cells in these groups of F-550 and F–Ti. Taking it further, we could find that the combination of nanotexture and

anatase exhibited inhibitory effect on the spreading and skeleton development shown in Fig. 8(c2) and (a2). However, when the annealing temperature increased to 900 °C, HASMCs attached on the surfaces of N-900 and F-900 were slenderer and more isolated compared with other samples, implying a significant inhibition of normal expressing of HASMCs, which mainly attributed to the formation of rutile and deteriorated surface morphology that reduced the effective area of cells attachment.

Nano- and micro-topography can regulate the biological behaviors of different types of cells, including endothelial cells (ECs), smooth muscle cells (SMCs). The direct effect of surface topography on the proliferation and phenotype of ECs and SMCs has been extensively discussed. Specifically, some studies have confirmed that highly ordered features, such as $TiO_2$ nanotube, can induce a decrease in the proliferation and cytoskeleton alignment of SMCs and an enhancement in ECs motility, proliferation, and migration [35,50]. Furthermore, nanotexture with special size could effectively stimulate or regulate several molecular adhesion and cellular events such as extracellular matrix protein secretion. Lee et al. [35] demonstrated that the amount of elastin and collagen produced by ECs cultured on regular nanotexture with the pore size of 110 nm were 6–8 and 2–3 times more than that of flat titanium surface, respectively. Collagen and elastin are necessary to form the ECM upon which they grow. As a result, the large amount of collagen and elastin under the simulation of nanotexture could provide a favorable microenvironment for ECs proliferation. Meanwhile, Peng et al. [51] reported that SMCs respond more effectively to submicrometric texture than nanoscale or microscale texture. The nanotextured surface could result in a decrease in SMCs proliferation and upregulate the expression of smooth muscle α-actin maintaining a differentiated state may aid in preventing disorder growth. As shown in Fig. 2, the pore size of regular nanotexture in the N–Ti and N-550 were approximately 100 ± 11 nm and 120 ± 7 nm, respectively. As stated above, it could provide a suitable nano-topography for promoting ECs growth and suppressing SMCs proliferation.

Furthermore, the crystal phase of metallic material also plays an important role in regulating biological response of cells [21]. For the $TiO_2$-based biomaterials, anatase and rutile are the two stable crystal phases of $TiO_2$, and both of them have semiconductor properties with band gap of 3.2 eV and 3.0 eV, respectively. Unlike the rutile phase, it could easily absorb visible light over a wider range of wavelength and excite electrons [39]. Anatase prevented the generation and transfer of electrons by reducing the likelihood of the photoelectric effect due to the high energy band gap than rutile, thus preventing the proteins adsorbed on the material surface from losing their original bioactivity or altering their function [52]. As shown in Figs. 5–8, HUVECs cultured on the surfaces of N-550 and F-550 present extensive filopodia and excellent spreading in multi-directions, indicating a great cellular adhesion and growth state. However, when the heat treatment temperature reached to 900 °C, the regular nanotexture completely disappeared companied by the generation of many refined rutile grains. One the one hand, micro-pits with lager size and irregular surface topography could not provide adequate effective contact area for the ECs and SMCs adhesion and proliferation. On the other hand, the abundant grain boundaries resulted in an increased specific surface area and surface energy shown in Table 1, providing more oxidation channels and active sites to react with biomolecules in the cells and thus inhibit cell activity [53]. As a result, HUVECs and HASMCs cultured on N-900 and F-900 all presented inactive growth behaviors.

### 3.5. Migration and proliferation behaviors of HUVECs and HASMCs

Migration ability of endothelial cells is another important indicator to evaluate the pro-endothelialization performance of modified surfaces. Meanwhile, suppressing the smooth muscle cell migration is equally crucial for preventing the tissue hyperplasia. Therefore, an idea modified surface is one that supports rapid endothelialization while reducing
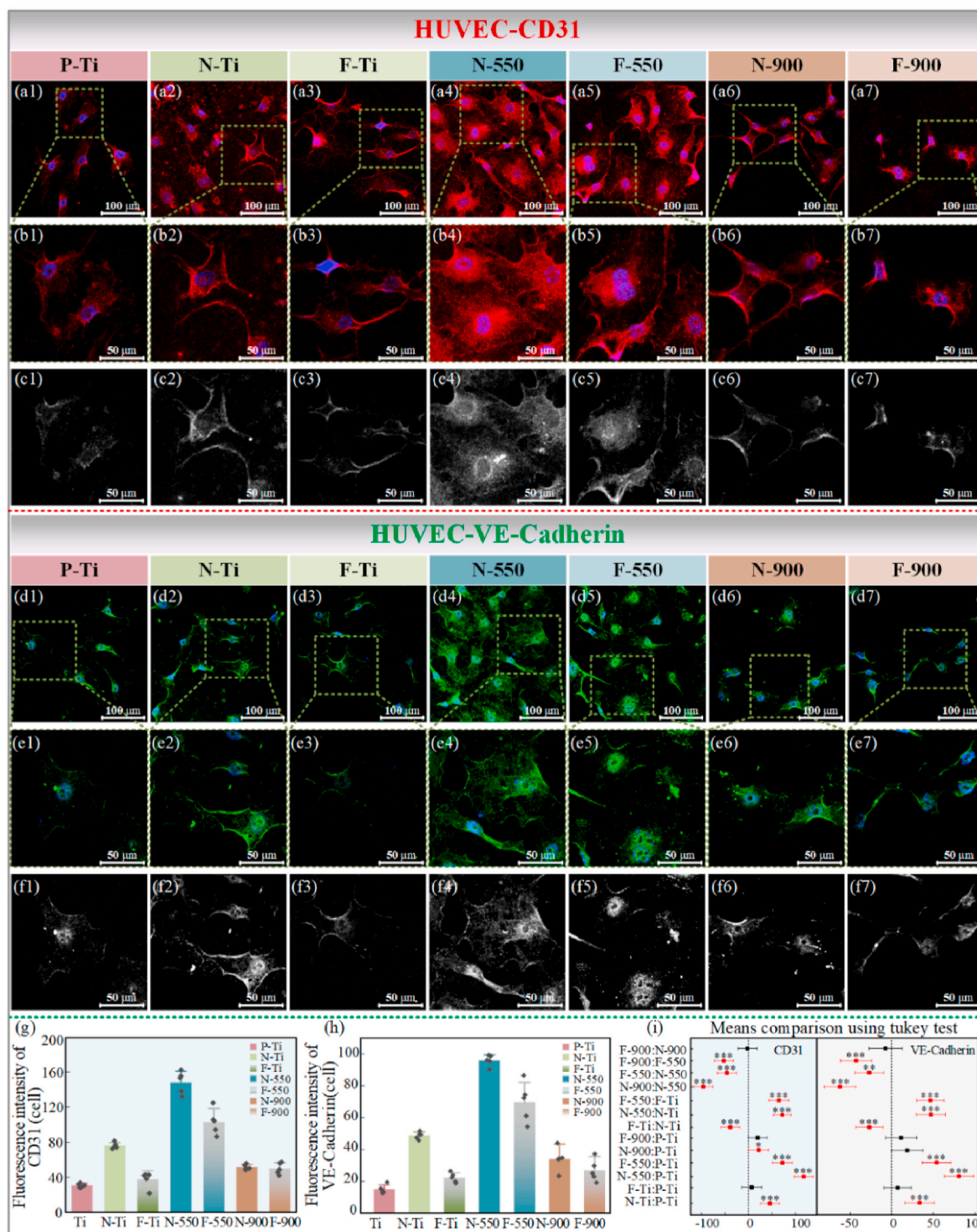
**Fig. 7.** Evaluation of endothelium quality and maturity based on the expression of CD31 and VE-Cadherin. **(a1-c7)** Immunofluorescence of CD31 in HUVECs cultured for 48 h on the surfaces of pure titanium (P–Ti), un-annealed nanotexture surface (N–Ti), un-annealed oxide layer surface (F–Ti), nanotexture surface annealed at 550 °C (N-550), oxide layer surface annealed at 550 °C (F-550), nanotexture surface annealed at 900 °C (N-900), oxide layer surface annealed at 900 °C (F-900); **(d1-f7)** Immunofluorescence of VE-Cadherin in HUVECs cultured for 48 h on the surfaces of P–Ti, N–Ti, F–Ti, N-550, F-550, N-900, and F-900; **(g)** Quantified fluorescence intensity of CD31 in HUVECs cultured on different sample surfaces for 48 h; **(h)** Quantified fluorescence intensity of VE-Cadherin in HUVECs cultured on different sample surfaces for 48 h; **(i)** Statistical analysis of CD31 and VE-Cadherin expression using one-way analysis of variance (ANOVA) followed by Tukey's post hoc test, $*P < 0.05$, $**P < 0.01$, $***P < 0.001$, (blue color denoted nucleus, red color denoted CD31, green color denoted VE-Cadherin). (For interpretation of the references to color in this figure legend, the reader is referred to the Web version of this article.)
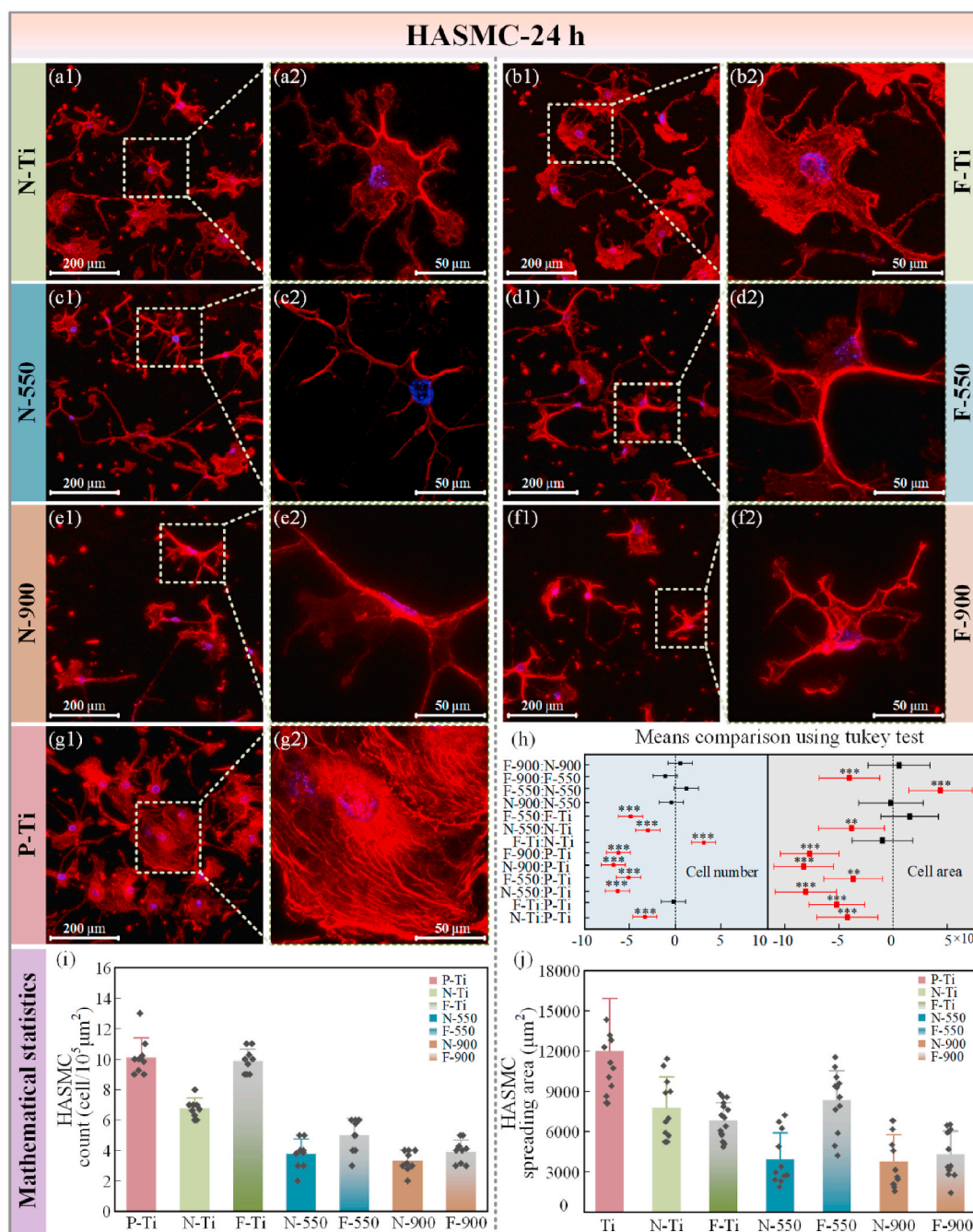
**Fig. 8.** Cytoskeletal actin stains and statistical analysis of HASMCs cultured on different samples surfaces for 24 h. **(a1-g2)** Fluorescent images of HASMCs attached on different sample surfaces; **(h)** Statistical analysis of adhered number and spreading area of HASMCs using one-way analysis of variance (ANOVA) followed by Tukey's post hoc test, *$P < 0.05$, * *$P < 0.01$, ***$P < 0.001$; **(i)** Amounts of HASMCs attached on the different samples surfaces; **(j)** Single-cell spreading area of HASMCs on different samples surfaces (Blue color denoted nucleus, red color denoted filamentous actin). (For interpretation of the references to color in this figure legend, the reader is referred to the Web version of this article.)

the migration rate of smooth muscle cell on the surface. As shown in Fig. 9(a1-a3) and (b1-b3), the migration distance and density of the HASMCs on the surfaces of P–Ti, N–Ti, and F–Ti did not present significant differences, while some differences can be observed in migration ability and proliferation density of HUVECs on these sample surfaces, implying that presence of nanotexture provided a friendly microenvironment for HUVECs attachment, cytoskeleton development, and rapidly migration. Furthermore, when the samples subjected to an annealing treatment at 550 °C, by comparing the migration distance and cells density on the surfaces of P–Ti, N–Ti and N-550, it could be found that HUVECs migration ability was greatly promoted while HASMCs

migration was obviously suppressed on the surface of N-550, which indicated that anatase produced positive effect on promoting HUVECs migration ability and inhibiting HASMCs proliferation. The biological effect induced by anatase could be also confirmed from the migration behavior of HUVECs and HASMCs on the surfaces of F-550 and F–Ti, where only crystal phase differed in the two groups. Moreover, the cells migration behaviors on the surfaces of N-550 and F-550 reflected that the biological effect induced solely by anatase was lower than what was triggered by the coupling of anatase and nanotexture. As shown in Fig. 9 (a4) and (b4), HUVECs showed the longest migration distance with the largest single cell spreading area and proliferation density on the surface
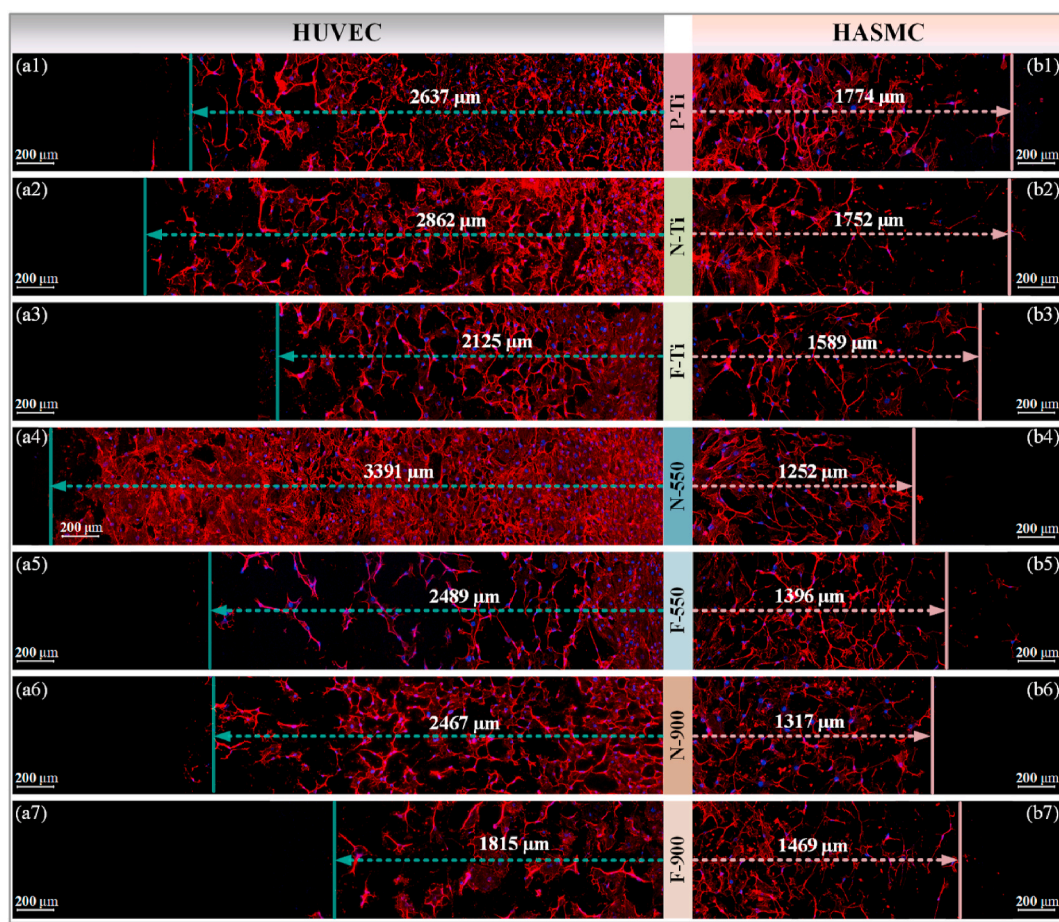
**Fig. 9.** Immunofluorescence staining micrographs of HUVECs and HASMCs migration on different sample surfaces after being cultured for 72 h. **(a1-a7)** Migration distance of HUVECs on the original pure titanium surface (P–Ti), un-annealed nanotexture surface (N–Ti); un-annealed oxide layer surface (F–Ti), nanotexture surface annealed at 550 °C (N-550), oxide layer surface annealed at 550 °C (F-550), nanotexture surface annealed at 900 °C (N-900), oxide layer surface annealed at 900 °C (F-900); **(b1-b7)** Migration distance of HUVECs on the surfaces of P–Ti, N–Ti, F–Ti, N-550, F-550, N-900, and F-900 (blue color denoted nucleus, red color denoted filamentous actin). (For interpretation of the references to color in this figure legend, the reader is referred to the Web version of this article.)

of N-550, whereas HASMCs presented the shortest migration distance. As discussed above, the regular nanotexture with size of 110–120 nm employed in the surface of N-550 could provide a suitable nano-topography for promoting ECs attachment, cytoskeleton development, and rapidly migration while suppressing SMCs proliferation [35,51]. Also, the anatase has a higher band gap compared to other crystal phase, which can effectively avoid electron spillover and transfer, preventing the proteins adsorbed on the material surface from losing their original bioactivity or altering their function, thereby also providing a stable and friendly microenvironment for cells growth [52]. Subsequently, when the annealing treatment temperature reached to 900 °C, both the migration distance and cells density on the surfaces of N-900 and F-900 were considerably lower than that of pure titanium, which indicated that the crystal phase transformation from anatase to rutile accompanied by the deteriorated surface morphology strongly inhibited HUVAECs and HASMCs migration ability.

### 3.6. Competitive proliferation behaviors of HUVECs and HASMCs

Enhancing the proliferative activity of HUVECs could accelerate wound healing resulting from vascular implant placement. However, the competitive effect of HUVECs with HASMCs *in vivo* cannot be ignored, and rapid HASMCs proliferation can also cause tissue disorderly hyperplasia on the implant surface. Separately analyzing the effect of the material properties on HUVECs proliferation, without considering the competition with HASMCs, may not be accurate to evaluate its

biocompatibility. Therefore, the competitive growth behavior between HUVECs and HASMCs on different sample surfaces were further analyzed by a long-term co-culture test. As an endothelial cell marker, CD31 is widely involved in growth behaviors of endothelial cells such as adhesion and migration and plays an important role in maintaining the integrity of endothelial cell junctions. α-SMA, a characteristic marker to distinguish the phenotype of vascular smooth muscle cells, performs important role in cell motility, structure, and integrity. Therefore, the competitive proliferation behaviors of endothelial cells and smooth muscle cells were distinguished and observed according to proteins expression of CD31 and α-SMA after co-culture on different modified surfaces for 7 days.

First, the cells morphology was observed after being cultured for 7 days. As shown in Fig. 10(a1-a5), After 7 days of co-culture on the surface of P–Ti, HASMCs proliferated substantially under the co-culture environment, far outnumbering endothelial cells, and a smaller number of HUVECs were observed from the profiles of the fluorescence image in which they were covered by HASMCs. In addition, immunofluorescence staining showed significant expression of α-SMA protein in HASMCs along with higher cells adhesion and proliferative activity, indicating that the growth of HASMCs was dominant in this competitive environment on the pure titanium surface. However, when the honeycomb nanotexture was fabricated on the pure titanium surface, i.e., N–Ti shown in Fig. 10(b1-b5), the number of CD31-labeled HUVECs increased while α-SMA-labeled HASMCs showed a significant decrease compared to that of P–Ti, which was consistent with the aforementioned results of
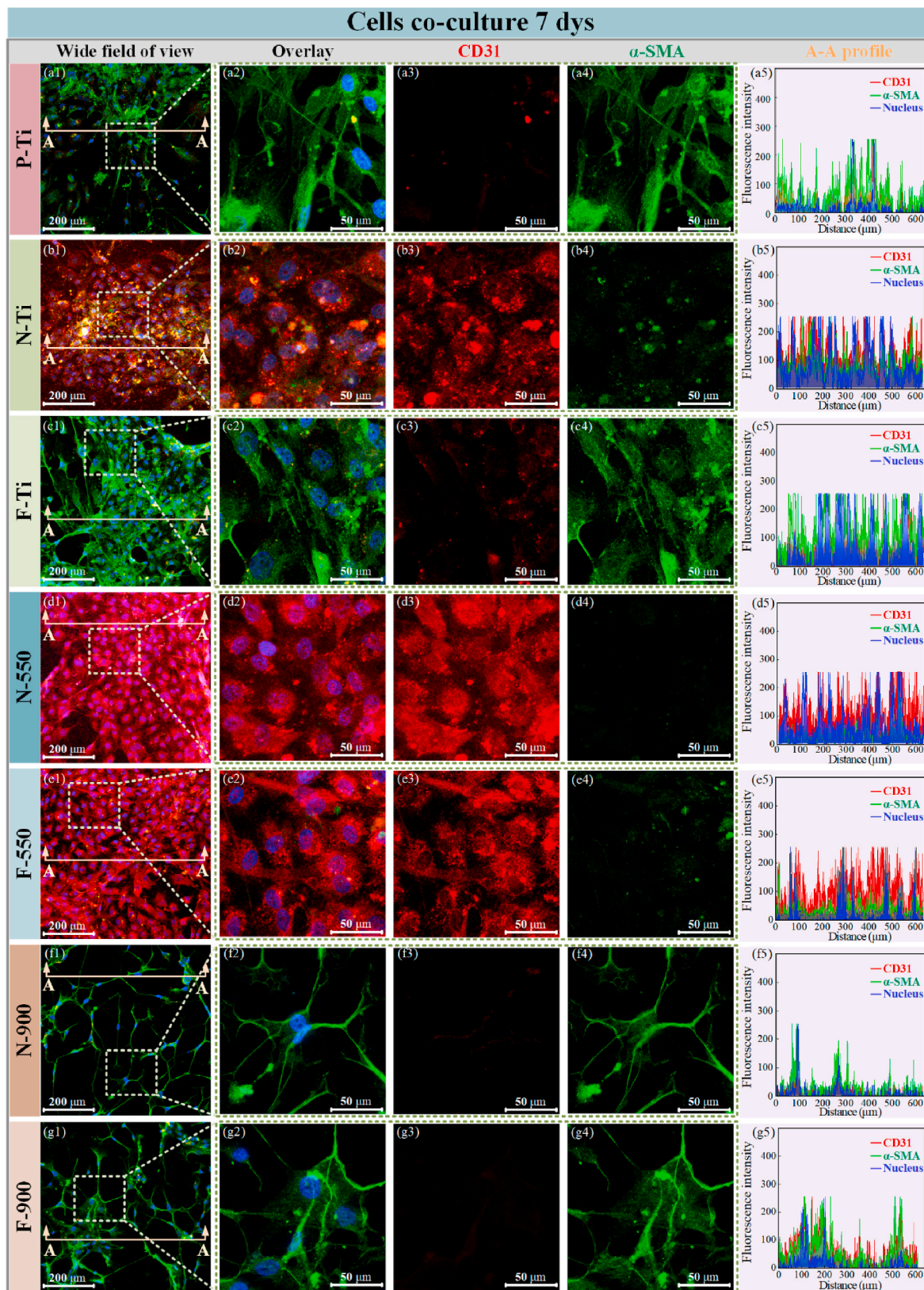
**Fig. 10.** Competitive adhesion and proliferation of HUVECs (red color denoted CD31 in HUVEC) and HASMCs (green color denoted α-SMA in HASMC) after co-culture on different sample surfaces for 7 days. **(a1)** Immunofluorescence images of CD31 and α-SMA expression in HUVECs and HASMCs co-cultured on the pure titanium surface (P–Ti) under a large field of view; **(a2-a4)** local details of competitive adhesion and proliferation behaviors of cells; **(a5)** Cells distribution analysis based on profiled view of cells adhesion layer on pure titanium surface; **(b1-b5)** Un-annealed nanotexture surface (N–Ti); **(c1-c5)** Un-annealed oxide layer surface (F–Ti); **(d1-d5)** Nanotexture surface annealed at 550 °C (N-550); **(e1-e5)** Oxide layer surface annealed at 550 °C (F-550); **(f1-f5)** Nanotexture surface annealed at 900 °C (N-900); **(g1-g5)** Oxide layer surface annealed at 900 °C (F-900). (For interpretation of the references to color in this figure legend, the reader is referred to the Web version of this article.)

individual cells adhesion, further suggesting that special nanotexture could contribute to the selective promotion of HUVECs proliferation and inhibition of HASMCs. Furthermore, when annealing treatment was performed at 550 °C, both N-550 and F-550 selectively and greatly promoted the attachment and spreading of HUVECs relative to HASMCs shown in Fig. 10(d1-d4). Especially for N-550, the CD31expression of HUVECs grown on the modified surface was remarkable and the cytoskeleton spread out sufficiently shown in Fig. 6(c1-c2). Meanwhile, the junction of cell-to-cell showed a tight morphology, which further

indicating that the combination of nanotexture and anatase phase could induce favorable biological responses in terms of HUVECs proliferation and facilitate the formation of integrated monolayers of endothelium. However, no obvious proliferation was observed on the surfaces of N-900 and F-900 for HUVECs and HASMCs, and the cytoskeleton of HASMCs exhibit a reticulately connected morphology that indicating an extremely inactive state of cells growth and proliferation due to the reduction of local adhesion caused by crystallographic properties of rutile phase and deteriorating surface topography.
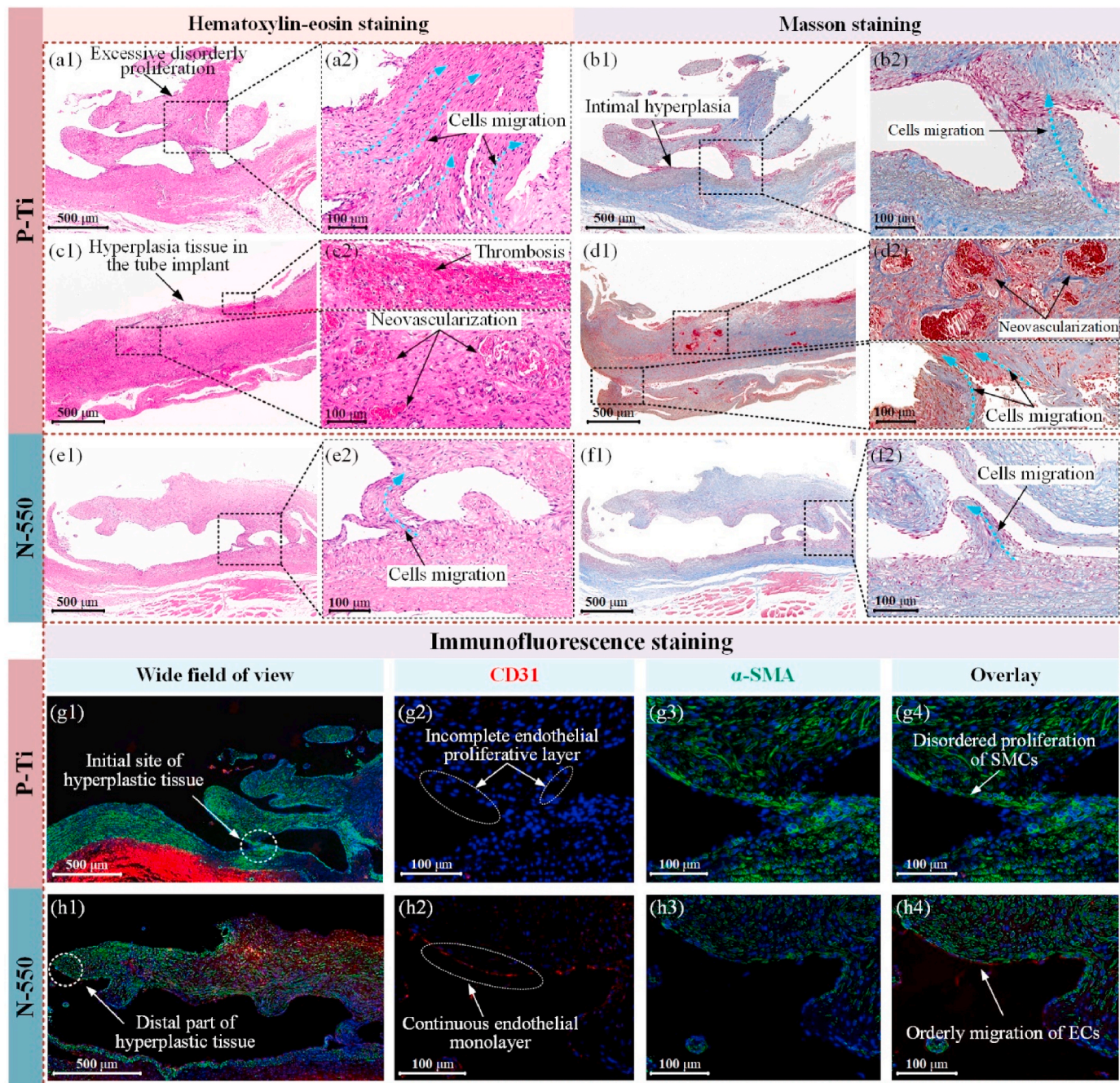


**Fig. 11.** Histopathological analysis of the blood vessel tissue and the hyperplasia tissue at the site of tube implants. **(a1-a2)** Hematoxylin-eosin (HE) staining of the blood vessel tissue at the site of P–Ti implant; **(b1-b2)** Masson staining of the blood vessel tissue; **(c1-c2)** HE staining of hyperplasia tissue generated in the lumen of P–Ti implant; **(d1-d2)** Masson staining of hyperplasia tissue generated in the lumen of P–Ti implant; **(e1-e2)** HE staining of the blood vessel tissue at the site of N-550 implant; **(f1-f2)** Masson staining of the blood vessel tissue; **(g1-g4)** Immunofluorescent staining of CD31 and α-SMA expressed in the blood vessel tissue at the site of P–Ti implant; **(h1-h4)** Immunofluorescent staining of CD31 and α-SMA expressed in the blood vessel tissue at the site of N-550 implant (blue color denoted nucleus, red color denoted CD31, green color denoted VE-Cadherin). (For interpretation of the references to color in this figure legend, the reader is referred to the Web version of this article.)

### 3.7. In vivo rapid endothelialization analysis of modified tube implants

Through analyzing the *in vitro* biological effects of different modified sample surfaces, the sample with honeycomb nanotexture annealed at 550 °C (N-550) showed excellent functions of selective pro-endothelialization and inhibition of SMCs proliferation. Therefore, the N-550 and pure titanium sample (P–Ti) were selected as the experimental group and control group during animal experiment to deeply analyze the synergistic regulation mechanism of vascular tissue cells adhesion and proliferation affected by nanotexture and crystal phase. One month after *in vivo* implantation, the small-diameter tube implants were removed from the left carotid artery. Histological staining including HE, Masson staining and immunofluorescence staining were carried out to further analyze the vascular remodeling and organization. Obviously, large amount of hyperplasia tissue generated in the lumens of P–Ti implant shown in Fig. 11(c1-d2), and obvious blood clots and some new capillaries appeared in the regenerated tissue, representing a high risk in eliciting thrombogenesis-resultant vascular occlusion. Additionally, as shown in Fig. 11(c2) and (d2), many fibroblasts and smooth muscle cells disorderly grew and some inflammatory cells infiltrated into hyperplasia tissue, and intimal thickening of the blood vessel at the site of implantation was particularly pronounced. By contrast, the luminal surface of N-550 implant was largely covered by a confluent and oriented cells without blood clots and new capillaries generated in the proliferated tissue. Compared to the disorganized hyperplasia tissue induced by P–Ti implant, the regenerated tissue layer on the surface of N-550 implant lumen exhibited an artery-like tissue with obvious cell orientation. As displayed in the HE and Masson staining images, well-organized elastin and collagen fibrillar formed in the regenerated tissue layer.

To analyze the rapid endothelialization on the luminal surfaces of tube implant, immunofluorescence staining of CD31 and α-SMA was performed. As shown in Fig. 11(g1-g4), strong positive expression of α-SMA protein revealed that the hyperplastic tissue of the vessel wall was filled with many smooth muscle cells in a disordered arrangement. Moreover, extremely low level of CD31 expression indicated that inefficient endothelialization capacity. Especially at the initial end of proliferative tissue (near the vessel wall) where an intact and continuous endothelial monolayer was still lacking. In contrast, as shown in Fig. 11 (h1-h4), an obvious confluent endothelial monolayer with strong positive expression of CD31 was visible even at the distal part of regenerated tissue layer, indicating the high efficiency of rapid endothelialization on the surface of N-550 implant. As a result, the rapid endothelialization rate effectively promoted the vascular remodeling and inhibited disordered tissue proliferation. In summary, *in vitro* and *in vivo* results showed that the special modification on the titanium surface was confirmed capable of programmatically regulating endothelium regeneration through guiding cell adhesion, promoting confluent endothelial monolayer formation, inducing endothelium maturation as well as suppressing disordered proliferation.

### 4. Conclusion

Selective pro-endothelialization and suppression of smooth muscle proliferation play a vital role in maintaining stable long-term service of blood-contacting implantable/interventional titanium devices. In this work, a novel strategy for fabricating the highly organized nanotexture on titanium substrate was proposed by a two-step anodic oxidation, combining an annealing treatment to achieve precise regulation of nanotexture topography and crystal phase. Among them, the morphological evolution of nanotexture is closely related to the transformation of the crystal phase. In particular, the phase transformation from anatase to rutile lead to the collapse of the regular honeycomb nanotexture, accompanied by the formation of fine rutile grains. The characterization of wettability and surface tension calculation showed that the presence of nanotexture reduced the surface tension of titanium, especially for the polar component, while the generation of anatase significantly enhanced the polar component of surface tension. Furthermore, rutile forming with deteriorated surface morphology reduced the effective area accessible to HUVECs and HASMCs attachment, thus hindering cells focal adhesion, cytoskeleton development and migration. By contrast, the combination of regular honeycomb nanotexture and anatase present positive effect on expression of CD31 and VE-Cadherin of ECs and provided a favorable microenvironment for HUVECs proliferation in a competitive with HASMCs. *In vivo* study further confirmed the modified tube implant with honeycomb nanotexture and anatase could facilitate rapid re-endothelialization, suppress neointimal disordered proliferation and reduce the risk of restenosis. The proposed modified strategy is hence believed to inspire the development and deployment of blood-contacting titanium implant to exploit their full potential.

### CRediT authorship contribution statement

**Jing Zhang:** Writing – review & editing, Writing – original draft, Visualization, Methodology, Investigation, Funding acquisition, Formal analysis, Data curation. **Kai Ren:** Writing – review & editing, Software, Investigation, Formal analysis, Data curation, Conceptualization. **Jingru Qiu:** Supervision, Software, Resources, Methodology. **Baolan Chen:** Software, Methodology, Data curation. **Weixun Duan:** Validation, Supervision, Resources, Methodology, Conceptualization. **Jincheng Liu:** Writing – review & editing, Resources, Project administration, Funding acquisition, Conceptualization. **Guiling Li:** Writing – review & editing, Supervision, Resources, Project administration, Methodology, Funding acquisition, Data curation, Conceptualization. **Donghai Li:** Writing – review & editing, Supervision, Resources, Project administration, Funding acquisition, Data curation, Conceptualization.

### Declaration of competing interest

The authors declare that they have no known competing financial interests or personal relationships that could have appeared to influence the work reported in this paper.

### Data availability

Data will be made available on request.

### Acknowledgements

### Appendix A. Supplementary data

Supplementary data to this article can be found online at https://doi.org/10.1016/j.mtbio.2024.100968.

# References

[1] G. Krenning, M.J.A. Van Luyn, M.C. Harmsen, Endothelial progenitor cell-based neovascularization: implications for therapy, Trends Mol. Med. 15 (2009) 180–189.

[2] R.A. Elsabbagh, M.F. Abdel Rahman, S.I. Hassanein, R.S. Hanafi, R.A. Assal, G.M. Shaban, M.Z. Gad, The association of megalin and cubilin genetic variants with serum levels of 25-hydroxvitamin d and the incidence of acute coronary syndrome in egyptians: a case control study, J. Adv. Res. 21 (2020) 49–56.

[3] D.E. Cutlip, S. Windecker, R. Mehran, A. Boam, D.J. Cohen, G.A. van Es, P.G. Steg, M. Morel, L. Mauri, P. Vranckx, E. McFadden, A. Lansky, M. Hamon, M. Krucoff, P. Serruys, Clinical end points in coronary stent trials: a case for standardized definitions, Circulation 115 (2007) 2344–2351.

[4] U. Sigwart, Drug-eluting stents are safe and effective: right or wrong? J. Am. Coll. Cardiol. 47 (2006) 1361–1362.

[5] Y. Hou, F. Witte, J. Li, S. Guan, The increased ratio of $Mg^{2+}/Ca^{2+}$ from degrading magnesium alloys directs macrophage fate for functionalized growth of endothelial cells, Smart Mater. Med. 3 (2022) 188–198.

[6] Z. Yang, S. Zhong, Y. Yang, M.F. Maitz, X. Li, Q. Tu, P. Qi, H. Zhang, H. Qiu, J. Wang, N. Huang, Polydopamine-mediated long-term elution of the direct thrombin inhibitor bivalirudin from $TiO_2$ nanotubes for improved vascular biocompatibility, J. Mater. Chem. B 2 (2014) 6767–6778.

[7] T. Liu, Y. Hu, J. Tan, S. Liu, J. Chen, X. Guo, C. Pan, X. Li, Surface biomimetic modification with laminin-loaded heparin/poly-l-lysine nanoparticles for improving the biocompatibility, Mater. Sci. Eng. C 71 (2017) 929–936.

[8] X. Zhou, Q. Gao, D. Yu, Y. Shao, Z. Wang, X. Liu, W. Wang, L. Chang, T. Ma, H. Mok, J. Cen, J. Chen, M.E. Tahchi, J. Zhuang, F. Mou, J. Zhang, Y. Yin, 3D-bioprinted vascular scaffold with tunable mechanical properties for simulating and promoting neo-vascularization, Smart Mater. Med. 3 (2022) 199–208.

[9] N. Lyu, Z. Du, H. Qiu, P. Gao, Q. Yao, K. Xiong, Q. Tu, X. Li, B. Chen, M. Wang, G. Pan, N. Huang, Z. Yang, Mimicking the nitric oxide-releasing and glycocalyx functions of endothelium on vascular stent surfaces, Adv. Sci. 8 (2021) 2101788.

[10] J. He, Q. Liu, S. Zheng, R. Shen, X. Wang, J. Gao, Q. Wang, J. Huang, J. Ding, Enlargement, reduction, and even reversal of relative migration speeds of endothelial and smooth muscle cells on biomaterials simply by adjusting RGD nanospacing, ACS Appl. Mater. Interfaces 13 (2021) 42344–42356.

[11] R. Mu, Y. Zhang, L. Yan, Z. Liao, Y. Yang, H. Su, L. Dong, C.A. Wang, "Bridge-Building" glycan scaffold mimicking microbial invasion for in situ endothelialization, Adv. Mater. 33 (2021) e2103490.

[12] B. Zhang, R. Yao, C. Hu, M.F. Maitz, H. Wu, K. Liu, L. Yang, R. Luo, Y. Wang, Epigallocatechin gallate mediated sandwich-like coating for mimicking endothelium with sustained therapeutic nitric oxide generation and heparin release, Biomaterials 269 (2021) 120418.

[13] X. Ding, W. Zhang, P. Xu, W. Feng, X. Tang, X. Yang, L. Wang, L. Li, Y. Huang, J. Ji, D. Chen, H. Liu, Y. Fan, The regulatory effect of braided silk fiber skeletons with differential porosities on in vivo vascular tissue regeneration and long-term patency, Research 2022 (2022) 9825237, 9825237.

[14] S. Jana, Endothelialization of cardiovascular devices, Acta Biomater. 99 (2019) 53–71.

[15] J. Zhao, Y. Feng, Surface engineering of cardiovascular devices for improved hemocompatibility and rapid endothelialization, Adv. Healthcare Mater. 9 (2020) e2000920.

[16] X. Ren, Y. Feng, J. Guo, H. Wang, Q. Li, J. Yang, X. Hao, J. Lv, N. Ma, W. Li, Surface modification and endothelialization of biomaterials as potential scaffolds for vascular tissue engineering applications, Chem. Soc. Rev. 44 (2015) 5680–5742.

[17] X. Ding, W. Chin, C.N. Lee, J.L. Hedrick, Y.Y. Yang, Peptide-functionalized polyurethane coatings prepared via grafting-to strategy to selectively promote endothelialization, Adv. Healthcare Mater. 7 (2018) 1700944.

[18] X. Li, J. Liu, T. Yang, H. Qiu, L. Lu, Q. Tu, K. Xiong, N. Huang, Z. Yang, Mussel-inspired "Built-Up" surface chemistry for combining nitric oxide catalytic and vascular cell selective properties, Biomaterials 241 (2020) 119904.

[19] C. Wang, H. Hao, J. Wang, Y. Xue, J. Huang, K. Ren, J. Ji, High-throughput hyaluronic acid hydrogel arrays for cell selective adhesion screening, J. Mater. Chem. B 9 (2021) 424–443.

[20] R. Zhou, Y. Wu, K. Chen, D. Zhang, Q. Chen, D. Zhang, Y. She, W. Zhang, L. Liu, Y. Zhu, C. Gao, R. Liu, A polymeric strategy empowering vascular cell selectivity and potential application superior to extracellular matrix peptides, Adv. Mater. 34 (2022) 2200464.

[21] C.C. Mohan, P.R. Sreerekha, V.V. Divyarani, S. Nair, K. Chennazhi, D. Menon, Influence of titania nanotopography on human vascular cell functionality and its proliferation in vitro, J. Mater. Chem. 22 (2012) 1326–1340.

[22] Y. Liu, K. Cheng, W. Weng, M. Yu, J. Lin, H. Wang, P. Du, G. Han, Influence of rod-surface structure on biological interactions between $TiO_2$ nanorod films and proteins/cells, Thin Solid Films 544 (2013) 285–290.

[23] M.F. Maitz, M.C.L. Martins, N. Grabow, C. Matschegewski, N. Huang, E.L. Chaikof, M.A. Barbosa, C. Werner, C. Sperling, The blood compatibility challenge. part 4: surface modification for hemocompatible materials: passive and active approaches to guide blood-material interactions, Acta Biomater. 94 (2019) 33–43.

[24] E.S. Bronze-Uhle, L.F.G. Dias, L.D. Trino, A.A. Matos, R.C. de Oliveira, P.N. Lisboa-Filho, Physicochemical characterization of albumin immobilized on different $TiO_2$ surfaces for use in implant materials, Colloids Surf., A 564 (2019) 39–50.

[25] K.S. Brammer, S. Oh, J.O. Gallagher, S. Jin, Enhanced cellular mobility guided by $TiO_2$ nanotube surfaces, Nano Lett. 8 (2008) 786–793.

[26] H.N. Pantaroto, J.M. Cordeiro, L.T. Pereira, A.B. de Almeida, F.H. Nociti Junior, E.C. Rangel, N.F. Azevedo Neto, J.H.D. da Silva, V.A.R. Barão, Sputtered crystalline $TiO_2$ film drives improved surface properties of titanium-based biomedical implants, Mater. Sci. Eng. C 119 (2021) 111638.

[27] C.C. Mohan, K.P. Chennazhi, D. Menon, In vitro hemocompatibility and vascular endothelial cell functionality on titania nanostructures under static and dynamic conditions for improved coronary stenting applications, Acta Biomater. 9 (2013) 9568–9577.

[28] A.M. Cherian, S.V. Nair, V. Maniyal, D. Menon, Surface engineering at the nanoscale: a way forward to improve coronary stent efficacy, APL Bioeng. 5 (2021) 021508.

[29] X. Zhang, X. Zheng, Y. Cheng, G. Li, X. Chen, J. Zheng, Formation of rutile fasciculate zone induced by sunlight irradiation at room temperature and its hemocompatibility, Mater. Sci. Eng. C 33 (2013) 3289–3293.

[30] Y. Suzuki, G. Ichihara, S. Kawada, K. Miyazawa, T. Furutani, A. Hayashida, E. Watanabe, C. Zong, L. Tran, A. Ikegami, S. Ichihara, Effects of physiochemical characteristic of nano-sized $TiO_2$ on the adhesion of monocytes to endothelial cells, NanoImpact 20 (2020) 100257.

[31] H. Nuhn, C.E. Blanco, T.A. Desai, Nanoengineered stent surface to reduce in-stent restenosis in vivo, ACS Appl. Mater. Interfaces 9 (2017) 19677–19686.

[32] M. Yu, Y. Lin, Y. Zhou, S. Jin, H. Cui, Q. Li, Z. Liu, L. Dong, K. Cheng, W. Weng, H. Wang, Enhanced osteointegration of hierarchical structured 3d-printed titanium implants, ACS Appl. Bio Mater. 1 (2018) 90–99.

[33] J. Xiong, T. Stehle, R. Zhang, A. Joachimiak, M. Frech, S.L. Goodman, M.A. Arnaout, Crystal structure of the extracellular segment of integrin alpha V beta 3 in complex with an Arg-Gly-Asp ligand, Science 296 (2002) 151–155.

[34] X. Wang, C. Yan, K. Ye, Y. He, Z. Li, J. Ding, Effect of RGD nanospacing on differentiation of stem cells, Biomaterials 34 (2013) 2865–2874.

[35] P.P. Lee, T.A. Desai, Nitinol-based nanotubular arrays with controlled diameters upregulate human vascular cell ECM production, ACS Biomater. Sci. Eng. 2 (2016) 409–414.

[36] I. Junkar, M. Kulkarni, M. Bencina, J. Kovac, K. Mrak-Poljsak, K. Lakota, S. Sodin-Semrl, M. Mozetic, A. Iglic, Titanium dioxide nanotube arrays for cardiovascular stent applications, ACS Omega 5 (2020) 7280–7289.

[37] Y.Z. Wang, Y.S. Wu, H. Yang, M. Wang, X.G. Shi, C. Wang, S.W. Zhang, Effect of calcination temperature on the microstructure and antimicrobial activity of boron and cerium co-doped titania nanomaterials, Mater. Technol. 33 (2018) 48–56.

[38] M.D. Roach, R.S. Williamson, I.P. Blakely, L.M. Didier, Tuning anatase and rutile phase ratios and nanoscale surface features by anodization processing onto titanium substrate surfaces, Mater. Sci. Eng. C 58 (2016) 213–223.

[39] D.A.H. Hanaor, C.C. Sorrell, Review of the anatase to rutile phase transformation, J. Mater. Sci. 46 (2011) 855–874.

[40] M. Batzill, E.H. Morales, U. Diebold, Influence of nitrogen doping on the defect formation and surface properties of $TiO_2$ rutile and anatase, Phys. Rev. Lett. 96 (2006) 026103.

[41] J. Zhang, G. Li, Y. Qu, Z. Guo, S. Zhang, D. Li, Fabrication and hemocompatibility evaluation of a robust honeycomb nanostructure on medical pure titanium surface, ACS Appl. Mater. Interfaces 14 (2022) 9807–9823.

[42] G. Mor, O. Varghese, M. Paulose, C. Grimes, Transparent highly ordered $TiO_2$ nanotube arrays via anodization of titanium thin films, Adv. Funct. Mater. 15 (2005) 1291–1296.

[43] Q. Huang, Y. Yang, D. Zheng, R. Song, Y. Zhang, P. Jiang, E.A. Vogler, C. Lin, Effect of construction of $TiO_2$ nanotubes on platelet behaviors: structure-property relationships, Acta Biomater. 51 (2017) 505–512.

[44] X. Zhang, X. Zhou, H. Xi, J. Sun, X. Liang, J. Wei, X. Xiao, Z. Liu, S. Li, Z. Liang, Y. Chen, Z. Wu, Interpretation of adhesion behaviors between bacteria and modified basalt fiber by surface thermodynamics and extended DLVO theory, Colloids Surf., B 177 (2019) 454–461.

[45] J.A. Brant, A.E. Childress, Assessing short-range membrane–colloid interactions using surface energetics, J. Membr. Sci. 203 (2002) 257–273.

[46] C.J. Van Oss, R.J. Good, M.K. Chaudhury, Additive and nonadditive surface tension components and the interpretation of contact angles, Langmuir 4 (1988) 884–891.

[47] C.J. van Oss, Acid-base interfacial interactions in aqueous media, Colloids Surf., A 78 (1993) 1–49.

[48] W. Cheng, X. Wang, Z. Xiong, J. Liu, Z. Liu, Y. Jin, H. Yao, T. Wong, J.S. Ho, B.C. K. Tee, Frictionless multiphasic interface for near-ideal aero-elastic pressure sensing, Nat. Mater. 22 (2023) 1352–1360.

[49] K. Anselme, Osteoblast adhesion on biomaterials, Biomaterials 21 (2000) 667–681.

[50] L. Peng, M.L. Eltgroth, T.J. LaTempa, C.A. Grimes, T.A. Desai, The effect of $TiO_2$ nanotubes on endothelial function and smooth muscle proliferation, Biomaterials 30 (2009) 1268–1272.

[51] L. Peng, A.J. Barczak, R.A. Barbeau, Y. Xiao, T.J. LaTempa, C.A. Grimes, T.A. Desai, Whole genome expression analysis reveals differential effects of $TiO_2$ nanotubes on vascular cells, Nano Lett. 10 (2010) 143–148.

[52] N. Huang, P. Yang, Y.X. Leng, J.Y. Chen, H. Sun, J. Wang, G.J. Wang, P.D. Ding, T. F. Xi, Y. Leng, Hemocompatibility of titanium oxide films, Biomaterials 24 (2003) 2177–2187.

[53] R. Huang, H. Zhuang, Y. Han, Second-phase-dependent grain refinement in Ti–25Nb–3Mo–3Zr–2Sn alloy and its enhanced osteoblast response, Mater. Sci. Eng. C 35 (2014) 144–152.